Published by
NIGERIAN SOCIETY OF PHYSICAL SCIENCES
Available online @ https://journal.nsps.org.ng/index.php/jnsps

J. Nig. Soc. Phys. Sci. 8 (2026) 3416

Check for updates

Journal of the Nigerian Society of Physical Sciences

Unsteady MHD Casson nanofluid transport over an inclined permeable cylinder in an anisotropic porous medium: effects of nonlinear radiation and Joule heating

Bukola Oluwatosin Falomo*, Olugbenga John Fenuga, Israel Olutunji Abiala

Department of Mathematics, University of Lagos, Lagos, Nigeria

Abstract

The present study investigates the coupled momentum, thermal, solutal, and magnetic transport characteristics of unsteady induced magnetohydrodynamic (MHD) Casson nanofluid flow over an inclined permeable cylindrical surface embedded in an anisotropic porous medium. The model incorporates several important physical mechanisms, including nonlinear thermal radiation, Joule heating, viscous dissipation, Brownian motion, thermophoresis, and higher-order chemical reaction kinetics. The governing nonlinear partial differential equations describing the conservation of mass, momentum, energy, nanoparticle concentration, and magnetic induction are transformed into a system of nonlinear ordinary differential equations through suitable similarity transformations derived using Lie group analysis. The resulting equations are solved using the semi-analytical homotopy perturbation method (HPM). The influence of key physical parameters on the velocity, temperature, nanoparticle concentration, and magnetic field profiles is analyzed through graphical and tabular results. The results indicate that increasing the magnetic parameter suppresses fluid motion due to the resistive Lorentz force while enhancing the thermal boundary layer thickness. The Casson parameter is found to significantly influence the velocity distribution, reflecting the non-Newtonian characteristics of the fluid. Thermal radiation and viscous dissipation increase the temperature field, whereas Brownian motion and thermophoresis strongly affect nanoparticle concentration profiles. Furthermore, anisotropic porous medium parameters and chemical reaction kinetics play important roles in controlling mass transfer rates. The study provides useful insights into magnetically controlled nanofluid transport in porous cylindrical geometries, which may assist in the design of advanced thermal systems in engineering applications.

DOI: 10.46481/jnsps.2026.3416

Keywords: Casson nanofluid, Inclined stretching cylinder, Anisotropic porous medium, Brownian motion, Homotopy perturbation method

Article History:
Received: 08 April 2026
Received in revised form: 11 July 2026
Accepted for publication: 13 July 2026
Available online: 12 August 2026

Communicated by: B. J. Falaye

Nomenclature

(r, θ, z) Coordinates along radial, circumferential and axial directions.

(v, w, u) Fluid velocity components along (r, θ, z).

P, p Fluid pressure; $P = p + \frac{B^2}{2\mu_m}$ (modified pressure).

μ_m, ν_m Magnetic permeability and magnetic diffusivity.

g, ρ_f, ρ_p Gravity acceleration, nanofluid density, nanoparticle density.

q_w, q_r Wall heat flux and radiative heat flux.

Γ, Z Porous medium parameter and scaled axial coordinate.

*Corresponding Author Tel. No.: +234-813-002-2746.

Email address: bukfalomo@gmail.com (Bukola Oluwatosin Falomo)

D_B, D_T Brownian motion and thermophoretic diffusivities.

B_z, B_r Components of induced magnetic field $\mathbf{B}$.

k_f, α_f, Sc Thermal conductivity, thermal diffusivity and Schmidt number.

j_w Nanofluid volume fraction flux at the wall.

A_t, f_w Unsteadiness parameter and surface mass flux.

ϕ, Q, n Volume fraction, Chandrasekhar number and temperature exponent.

Ω, Λ Velocity ratio and inverse magnetic Prandtl number.

(ν, ν') Kinematic and viscoelastic viscosities.

(μ, μ', ς) Dynamic and viscoelastic viscosities, transformed coordinate.

β_p, Da, β Viscoelastic parameter, Darcy number and Casson parameter.

R_d, Ri, N_r Radiation parameter, Richardson number and buoyancy ratio.

Ec, Pr, Le Eckert, Prandtl and Lewis numbers.

γ Curvature parameter.

$(\rho c)_f, (\rho c)_p$ Heat capacities of fluid and nanoparticles.

N_b, N_t Brownian motion and thermophoresis parameters.

Q_0, ϖ Heat generation coefficient and exponent.

κ_r, κ^2 Chemical reaction rate and parameter.

Bi, h_f Biot number and heat transfer coefficient.

σ^*, k^*, s^* Stefan-Boltzmann constant, absorption and scattering coefficients.

T, ϑ, T_∞ Temperature, dimensionless concentration and ambient temperature.

1. Introduction

Transport processes involving heat, momentum, and mass transfer play a fundamental role in numerous engineering and industrial systems, including polymer processing, cooling technologies, nuclear reactors, geothermal energy extraction, biomedical transport processes, and chemical reactors. Efficient thermal management in such systems remains a major challenge because conventional fluids often exhibit limited thermal conductivity. To address this limitation, nanofluids, which are engineered suspensions of nanoparticles dispersed in base fluids, have been introduced as advanced heat-transfer fluids [1]. Nanoparticles significantly enhance the effective thermal conductivity of the base fluid and improve convective heat transfer performance in many practical applications.

The theoretical understanding of nanofluid transport mechanisms was significantly advanced by the model proposed by Buongiorno, which showed that Brownian diffusion and thermophoresis are the dominant mechanisms governing nanoparticle transport in convective flows [2]. These mechanisms strongly influence the temperature and concentration boundary layers in nanofluid systems and therefore play a crucial role in heat and mass transfer processes. Consequently, numerous investigations have explored nanofluid transport in boundary-layer flows over stretching surfaces, porous media, and other complex geometries [3,4,5,6].

In many practical situations, the working fluids exhibit non-Newtonian rheological behavior rather than classical Newtonian characteristics. Non-Newtonian fluids are frequently encountered in materials such as polymer melts, paints, biological fluids, and food products. Among various non-Newtonian models, the Casson fluid model has received considerable attention because it effectively captures yield stress behavior observed in fluids such as blood and pigment suspensions [7]. Because of its relevance in industrial and biomedical applications, the Casson model has been widely employed in the analysis of non-Newtonian boundary-layer flows and heat transfer processes [8,9].

Another important mechanism influencing fluid transport is the presence of magnetic fields. The study of electrically conducting fluids subjected to magnetic fields is known as magnetohydrodynamics (MHD). Magnetohydrodynamic flows arise in several technological applications including electromagnetic pumps, liquid metal cooling systems, crystal growth processes, and plasma physics. When a magnetic field interacts with an electrically conducting fluid, a Lorentz force is generated that resists fluid motion and modifies heat transfer characteristics [10]. As a result, magnetic fields can be used to regulate flow behavior and control thermal transport in engineering systems.

A classical problem in fluid mechanics that has attracted considerable attention is the boundary layer flow induced by stretching surfaces. Such flows arise in industrial processes including polymer extrusion, glass manufacturing, metal spinning, and continuous casting. The pioneering study by Crane provided an exact similarity solution for laminar boundary-layer flow over a linearly stretching sheet [11]. Since then, numerous investigations have extended this model to include additional physical effects such as magnetic fields, viscous dissipation, thermal radiation, and porous media [4,12,13,14].

The influence of porous media on fluid transport has also attracted substantial attention because porous materials appear in many natural and industrial systems such as geothermal reservoirs, petroleum extraction processes, filtration devices, and catalytic reactors. Fluid motion through porous structures is strongly influenced by the permeability of the medium. In many practical situations, porous materials exhibit anisotropic permeability, meaning that the permeability varies with direction. This anisotropic behavior significantly modifies the velocity distribution and energy transport characteristics of the flow.

In addition to porous medium effects, thermal radiation and Joule heating can significantly affect heat transfer in high-temperature environments. Radiative heat transfer becomes important in systems such as gas turbines, nuclear reactors, and combustion chambers. Several studies have incorporated nonlinear radiation models and Joule heating effects to better represent energy transport in magnetohydrodynamic nanofluid systems [15,16,17]. These studies show that radiation can increase fluid temperature while Joule heating contributes additional thermal energy to the system.

Recent studies have also focused on hybrid nanofluids and advanced nanofluid models, where multiple nanoparticle types are suspended in base fluids to enhance heat transfer performance. Experimental and theoretical investigations have shown that hybrid nanofluids can significantly improve thermal conductivity and heat transfer rates compared with single-component nanofluids [18,14,19]. Similarly, several recent investigations have examined nanofluid transport in magnetohydrodynamic boundary layer flows over stretching surfaces with radiation, chemical reaction, and porous medium effects [20].

More recent research between 2024 and 2025 has focused on complex nanofluid models involving Casson rheology, porous media, and magnetic fields. For example, studies have examined Casson nanofluid flow over stretching surfaces under the influence of thermal radiation, chemical reactions, and Joule heating [21,22]. These investigations show that magnetic forces significantly suppress fluid velocity while increasing thermal boundary-layer thickness due to the resistive Lorentz force acting on the fluid.

Similarly, several recent investigations have explored nanofluid transport in porous stretching surfaces and reported that parameters such as radiation, heat generation, and chemical reactions strongly influence heat and mass transfer rates [20,23]. These studies typically employ similarity transformations to convert the governing partial differential equations into ordinary differential equations that can be solved numerically or analytically.

Despite the extensive literature on nanofluid transport in magnetohydrodynamic boundary-layer flows, relatively few studies have examined unsteady Casson nanofluid flow over inclined cylindrical geometries embedded in anisotropic porous media with induced magnetic field effects. Cylindrical geometries are frequently encountered in engineering applications such as pipelines, heat exchangers, catalytic reactors, and energy transport devices. The combined effects of curvature, porous medium anisotropy, radiation, Joule heating, and chemical reaction introduce additional complexity into the governing transport equations.

Therefore, the major gap in the literature lies in the limited investigation of unsteady Casson nanofluid transport around an inclined permeable cylinder embedded in anisotropic porous medium under induced magnetohydrodynamic effects.

Motivated by this gap, the present study investigates coupled thermal and solutal transport in unsteady induced magnetohydrodynamic Casson nanofluid flow over inclined permeable cylinders embedded in anisotropic porous media. The model incorporates several important physical mechanisms including Brownian motion, thermophoresis, nonlinear radiation, viscous dissipation, Joule heating, and higher-order chemical reaction kinetics. The governing equations describing mass, momentum, energy, nanoparticle concentration, and magnetic induction are formulated using boundary-layer approximations and subsequently transformed into nonlinear ordinary differential equations using suitable similarity transformations.

The resulting system is solved using a semi-analytical technique to analyze the influence of key dimensionless parameters on velocity, temperature, nanoparticle concentration, and magnetic field distributions. The results obtained in this study provide valuable insights into magnetically controlled nanofluid transport in porous media environments and may assist in the design of advanced thermal systems used in industrial heat-transfer applications.

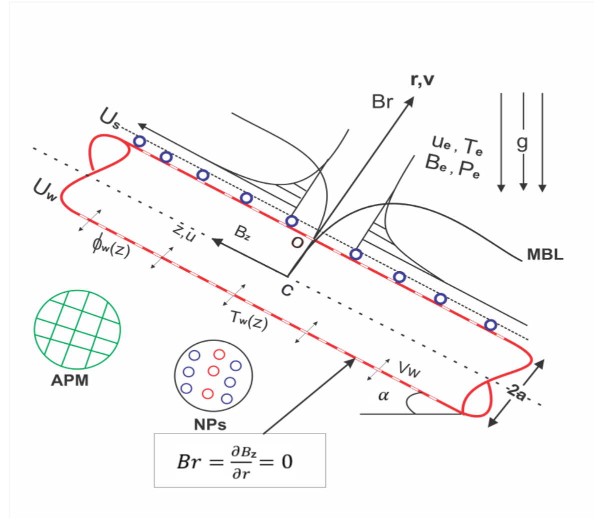

Figure 1: Schematic of the physical flow configuration.

2. Formulation of the problem

In this section, the mathematical model describing the physical configuration of the problem is developed. The study considers unsteady two-dimensional boundary-layer flow of an incompressible electrically conducting Casson nanofluid over an inclined permeable cylindrical surface embedded in an anisotropic porous medium under the influence of an induced magnetic field. The physical configuration of the flow system is illustrated schematically in Figure 1.

The cylindrical surface is assumed to stretch linearly along the axial direction, thereby generating a boundary-layer flow in the surrounding nanofluid. The coordinate system is chosen such that the axial coordinate z is aligned along the surface of the cylinder while the radial coordinate r is measured outward from the cylindrical surface. The corresponding velocity components of the fluid are denoted by u and v in the axial and radial directions, respectively.

The fluid is assumed to be laminar, incompressible, and electrically conducting. The base fluid and nanoparticles are assumed to be in thermal equilibrium, and the nanoparticle suspension is considered sufficiently dilute so that particle agglomeration and sedimentation effects are negligible. The influence of magnetic polarization is ignored, while the induced magnetic

Table 1: Comparison of the present results with Ref. [24] together with the (%) relative error.

β	N_b	N_t	κ^2	Ref. [24]			Present Study			(%) Relative Error		
				$-f''(0)$	$\theta(0)$	$\phi(0)$	$-f''(0)$	$\theta(0)$	$\phi(0)$	$-f''(0)$	$\theta(0)$	$\phi(0)$
0.10	0.10	0.30	0.20	0.651652	0.291163	0.275213	0.651763	0.290584	0.275011	0.0170	0.1989	0.0734
0.11				0.671211	0.291542	0.275831	0.671071	0.291342	0.275720	0.0209	0.0686	0.0403
0.12				0.688834	0.292427	0.277281	0.689450	0.292070	0.276392	0.0894	0.1221	0.3206
0.10	0.10	0.10		0.652317	0.273112	0.138951	0.651763	0.272612	0.138840	0.0849	0.1831	0.0800
	0.20	0.20		0.652317	0.311654	0.372417	0.651763	0.309713	0.371856	0.0849	0.6228	0.1506
	0.30	0.30		0.652317	0.363216	0.435548	0.651763	0.362584	0.435454	0.0849	0.1740	0.0217
	0.10		0.00	0.652317	0.301158	0.370652	0.651763	0.291841	0.366511	0.0849	3.0932	1.1172
			0.50	0.652317	0.290651	0.199105	0.651763	0.289571	0.198361	0.0849	0.3717	0.3738
			1.00	0.652317	0.289241	0.135237	0.651763	0.288769	0.133835	0.0849	0.1632	1.0367

field is incorporated into the model. Furthermore, the effects of Hall current and ion-slip are neglected for simplicity.

The porous medium in which the cylinder is embedded is assumed to possess anisotropic permeability, which introduces additional resistance to fluid motion. The Oberbeck–Boussinesq approximation is employed to account for density variations in the buoyancy term of the momentum equation while all other thermophysical properties are assumed constant. Thermal radiation effects are modeled using the Rosseland diffusion approximation, which is suitable for optically thick media.

Under the above assumptions, the governing equations describing the conservation of mass, momentum, thermal energy, nanoparticle concentration, and magnetic induction can be expressed in cylindrical coordinates. The continuity equation and the magnetic solenoidal condition take the forms

$$\frac{\partial(rv)}{\partial r} + \frac{\partial(ru)}{\partial z} = 0, \tag{1}$$

$$\frac{\partial(rB_r)}{\partial r} + \frac{\partial(rB_z)}{\partial z} = 0, \tag{2}$$

where $\mathbf{B} = (B_r, B_z)$ is the induced magnetic field.

The momentum equation for the Casson nanofluid is derived from the boundary-layer form of the Navier–Stokes equations while incorporating the effects of buoyancy forces, porous medium resistance, and magnetic body forces. The energy equation includes the effects of thermal conduction, viscous dissipation, Joule heating, nonlinear thermal radiation, and nanoparticle transport mechanisms. The nanoparticle concentration equation accounts for Brownian diffusion, thermophoretic diffusion, and higher-order chemical reaction kinetics. Additionally, the magnetic induction equation describes the evolution of the induced magnetic field within the conducting fluid.

The corresponding boundary conditions describe the stretching velocity of the cylinder surface, the prescribed temperature and nanoparticle concentration at the wall, and the asymptotic behavior of the velocity, temperature, concentration, and magnetic field far from the surface.

To simplify the mathematical formulation and obtain similarity solutions, appropriate similarity transformations are introduced. These transformations convert the governing partial differential equations into a system of nonlinear ordinary differential equations. The transformed equations depend on several dimensionless parameters such as the Casson parameter, curvature parameter, Chandrasekhar number, radiation parameter, Prandtl number, Brownian motion parameter, thermophoresis parameter, Schmidt number, Lewis number, and chemical reaction parameter.

Table 2: Comparison of $-f''(0)$ and $\theta'(0)$ for different values of γ and Pr.

γ	Pr	$-f''(0)$		$\theta'(0)$		
		Ref. [11]	Present	Ref. [25]	Ref. [26]	Present
0	0.72	1.0000	1.000000	1.2253	1.2367	1.236649
	1	(exact)	1.000000	1.0000	1.0000	1.000000
	6.7		1.000000	–	0.3333	0.333303
	10		1.000000	0.2688	0.2688	0.268769
0.5	0.72		1.180665			1.005806
	1		1.180665			0.84698
	6.7		1.180665			0.3133686
	10		1.180665			0.255784
1	0.72		1.353302		0.8701	0.853168
	1		1.353302		0.7439	0.738933
	6.7		1.353302		0.2966	0.296835
	10		1.353302		0.2442	0.244307

The resulting dimensionless equations together with the associated boundary conditions provide the mathematical framework used to analyze the coupled momentum, heat, mass, and magnetic transport processes in the present study.

$$\begin{aligned}\frac{\partial u}{\partial t} + \left(u\frac{\partial}{\partial z} + v\frac{\partial}{\partial r}\right)u = \frac{1}{\rho_f}\bigg[-\frac{\partial p}{\partial z} \\ + \mu\left(1+\frac{1}{\beta}\right)\nabla^2 u + F_z - \frac{\mu}{\rho_f K_2}\Gamma\left(K^*,\vartheta\right)\left(1+\frac{1}{\beta}\right)u\bigg],\end{aligned} \tag{3}$$

where the axial component of the resultant body force is

$$\begin{aligned}F_z = \left[-(\rho_p-\rho_f)(\phi-\phi_\infty) + (1-\phi_\infty)\rho_f\left(\beta_T(T-T_\infty)\right)\right] g\sin(\alpha) \\ + \frac{1}{\mu_m}\left(B_r\frac{\partial B_z}{\partial r} + B_z\frac{\partial B_z}{\partial z}\right),\end{aligned}$$

Table 3: Influence of β, ς, f_w, γ, Q, Z, Ω, Ri on $-Re_z^{\frac{1}{2}}C_f$, $Re_z^{-\frac{1}{2}}Nu_z$, and $Re_z^{-\frac{1}{2}}Sh_z$.

β	ζ	f_w	γ	Q	Z	Ω	Ri	$-Re_z^{\frac{1}{2}}C_f$	$Re_z^{-\frac{1}{2}}Nu_z$	$Re_z^{-\frac{1}{2}}Sh_z$
∞	0.1	-0.1	0.3	0.2	0.1	0.1	0.3	10.333373	0.915885	0.499574
1								7.301957	0.921104	0.502420
0.1								3.206587	0.911075	0.496950
	0							3.351918	0.934470	0.509711
0.2	0.1							2.334257	0.919071	0.501312
	0.2							1.812618	0.906615	0.494517
	0.1	-0.1						2.334257	0.919071	0.501312
		0						2.306683	0.911739	0.497312
		0.1						2.279167	0.904092	0.493141
		-0.1	0					1.871778	0.911494	0.497179
			0.1					2.033062	0.914162	0.498634
			0.2					2.187149	0.916645	0.499988
			0.3	0				2.275690	0.904220	0.493211
				0.2				2.279167	0.904092	0.493141
				0.4				2.282645	0.903963	0.493071
				0.2	0.1			2.279167	0.904092	0.493141
					0.3			2.307110	0.903118	0.492610
					0.5			2.363403	0.901074	0.491495
					0.1	0.1		2.334257	0.919071	0.501312
						0.3		2.097257	0.925397	0.504762
						0.5		1.739314	0.933119	0.508974
						0.1	0.1	2.362659	0.918473	0.500985
							0.3	2.334257	0.919071	0.501312
							0.5	2.306159	0.919654	0.501630

$$(\rho C)_f\left(\frac{\partial T}{\partial t}+u\frac{\partial T}{\partial z}+v\frac{\partial T}{\partial r}\right)=k_f\nabla^2T-\frac{1}{r}\frac{\partial}{\partial r}(rq_r)$$
$$+\mu\left(1+\frac{1}{\beta}\right)\left(\frac{\partial u}{\partial r}\right)^2+Q_0(T-T_\infty)^{\varpi} \tag{4}$$
$$+(\rho C)_p\left[D_B\nabla\phi\cdot\nabla T+\frac{D_T}{T_\infty}\nabla T\cdot\nabla T\right]+\frac{1}{\sigma}J^2,$$

where $q_r=-\dfrac{4\sigma^*}{3(k^*+s^*)}\dfrac{\partial T^4}{\partial r}$ (radiation heat flux). σ^*, k^*, s^* are respectively the Stefan-Boltzmann constants, the Rosseland mean absorption and scattering coefficients. Expanding T^4 by means of the Taylor theorem about the free stream temperature T_∞ and neglecting higher order terms, we obtain $T^4\cong 4T_\infty^3T-3T_\infty^4$ (see Ref. [27]). Neglecting s^* for non-scattering thin fluid, and substituting T^4 we have, $q_r=-\dfrac{16\sigma^*}{3k^*}T_\infty^3\dfrac{\partial T}{\partial r}$

$$\left(\frac{\partial}{\partial t}+u\frac{\partial}{\partial z}+v\frac{\partial}{\partial r}\right)\phi=D_B\frac{1}{r}\frac{\partial}{\partial r}\left(r\frac{\partial\phi}{\partial r}\right)$$
$$+\frac{D_T}{T_\infty}\frac{1}{r}\frac{\partial}{\partial r}\left(r\frac{\partial T}{\partial r}\right)$$
$$-\kappa_r(\phi-\phi_\infty)^m, \tag{5}$$

$$\left(\frac{\partial}{\partial t}+u\frac{\partial}{\partial z}+v\frac{\partial}{\partial r}\right)B_z=B_z\frac{\partial u}{\partial z}+B_r\frac{\partial u}{\partial r}+\frac{\eta_m}{r}\frac{\partial}{\partial r}\left(r\frac{\partial B_z}{\partial r}\right). \tag{6}$$

The initial and boundary conditions are [28,29]:

$$t\le 0:\quad u=v=0,\quad T=T_\infty,\quad \phi=\phi_\infty,$$
$$\mathbf{B}=(0,B_e(t,z)),\quad \text{for all } (r,\vartheta,z)\in\mathbb{R}^3,$$
$$\text{where}\quad B_z=B_e(t,z)=B_0\left(\frac{z}{l\,|1-\lambda t|}\right). \tag{7}$$

$$t>0:\quad u=U_w(t,z),\quad v=V_w(t,z),$$
$$T=T_w(t,z)=T_\infty+\frac{b_1z^n}{|1-\lambda t|},$$
$$\phi=\phi_w(t,z)=\phi_\infty+\frac{b_0z^n}{|1-\lambda t|},$$
$$B_r=\frac{\partial B_z}{\partial r}=0\quad\text{at } r=a,$$
$$u=u_e(t,z)\to 0,\quad \frac{\partial u}{\partial r}\to 0,\quad T\to T_\infty,$$
$$B_z\to B_e(t,z)=B_0\left(\frac{z}{l|1-\lambda t|}\right),\quad \phi\to\phi_\infty\quad\text{as } r\to\infty. \tag{8}$$

Table 4: Effects of N_r, Γ, D_a, R_d, P_r, E_c, G and ϖ on $-Re_z^{\frac{1}{2}}C_f$, $Re_z^{-\frac{1}{2}}Nu_z$, and $Re_z^{-\frac{1}{2}}Sh_z$.

N_r	Γ	D_a	R_d	P_r	E_c	G	ϖ	$-Re_z^{\frac{1}{2}}C_f$	$Re_z^{-\frac{1}{2}}Nu_z$	$Re_z^{-\frac{1}{2}}Sh_z$
0	0.3	0.1	0.1	1	0.01	0.1	1	2.350 989	0.918 716	0.501 118
0.2								2.334 257	0.919 071	0.501 312
0.4								2.317 553	0.919 423	0.501 504
0.2	0							2.245 633	0.921 036	0.502 383
	1							2.518 527	0.914 786	0.498 974
	2							2.740 148	0.909 268	0.495 965
	0.3	0						2.245 633	0.921 036	0.502 383
		0.2						2.416 755	0.917 186	0.500 283
		0.4						2.566 308	0.913 630	0.498 344
		0.1	0					2.336 225	1.010 484	0.505 242
			0.1					2.334 257	1.002 623	0.501 312
			0.2					2.332 335	0.995 237	0.497 619
			0.1	1				2.334 257	0.919 071	0.501 312
				2				2.344 067	0.966 246	0.527 043
				3				2.347 324	0.988 412	0.539 134
				1	0			2.335 654	0.924 021	0.504 012
					0.01			2.334 257	0.919 071	0.501 312
					0.02			2.332 861	0.914 130	0.498 616
					0.01	-0.1		2.338 112	0.934 153	0.509 538
						0		2.336 389	0.927 235	0.505 765
						0.1		2.334 257	0.919 071	0.501 312
						0.1	0	2.252 482	0.760 316	0.414 718
							1	2.334 257	0.919 071	0.501 312
							2	2.336 257	0.926 546	0.505 389

Introducing the following similarity transformations

$$\begin{aligned}
&\eta = \frac{r^2 - a^2}{2a}\sqrt{\frac{U_w}{\nu z}},\\
&u_z \equiv u = U_w f'(\eta), \quad u_r \equiv v = -\frac{a}{r}\sqrt{\frac{\nu U_w}{z}}\, f(\eta),\\
&\theta = \frac{T - T_\infty}{T_w - T_\infty}, \quad \varphi = \frac{\phi - \phi_\infty}{\phi_w - \phi_\infty},\\
&B_z = B_0\left(\frac{z}{a}\right)h'(\eta), \quad B_r = -\frac{B_0}{r}\sqrt{\frac{\nu z}{U_w}}\, h(\eta),\\
&U_w = U\left(\frac{z}{l\,|1-\lambda t|}\right), \quad a \neq 0,
\end{aligned} \tag{9}$$

where the quantity $\frac{z}{|1-\lambda t|}$ characterizes the unsteady stretching of the cylinder by coupling the axial coordinate with time. This scaling accounts for the temporal variation of the stretching rate and facilitates the reduction of the governing equations to a self-similar system of ordinary differential equations.

The similarity transformations introduced in equation (9), which satisfy both the continuity equation and the solenoidal condition for the induced magnetic field (see Ref. [30]), are employed to transform the governing partial differential equations into the following system of coupled nonlinear ordinary differential equations governing momentum, energy, chemically reactive nanoparticle transport, and magnetic induction:

$$\begin{aligned}
&\left(1+\frac{1}{\beta}\right)\left[(1+2\gamma\eta)f''' + 2\gamma f''\right] + ff'' - (f')^2 + Ri\,(\theta - N_r\varphi)\\
&-\Gamma Da\left(1+\frac{1}{\beta}\right)(f' - \Omega) + QZ^2\left(h'^2 - hh'' - 1\right) + A\Omega + \Omega^2 = 0,
\end{aligned} \tag{10}$$

$$\begin{aligned}
&\frac{1}{Pr}(1+R_d)\left[(1+2\gamma\eta)\theta'' + 2\gamma\theta'\right] + Ec\left(1+\frac{1}{\beta}\right)(1+2\gamma\eta)(f'')^2\\
&+ f\theta' - nf'\theta + G\theta^{\varpi} + (1+2\gamma\eta)\left[N_b\varphi'\theta' + N_t(\theta')^2\right]\\
&+ Q\Lambda Ec(h'')^2 = 0,
\end{aligned} \tag{11}$$

$$\begin{aligned}
&\frac{1}{Sc}\left[(1+2\gamma\eta)\varphi'' + 2\gamma\varphi'\right] + f\varphi' - nf'\varphi\\
&+ \frac{1}{Le\,Pr}\frac{N_t}{N_b}\left[(1+2\gamma\eta)\theta'' + 2\gamma\theta'\right] - \kappa^2\varphi^m = 0,
\end{aligned} \tag{12}$$

$$\Lambda\left\{(1+2\gamma\eta)h''' + 2\gamma h''\right\} + fh'' - hf'' - A_t\left(h' + \frac{1}{2}\eta h''\right) = 0. \tag{13}$$

Table 5: Influence of Bi, N_b, N_t, Λ, n, S_c, L_e, and κ^2 on $-Re_z^{\frac{1}{2}}C_f$, $Re_z^{-\frac{1}{2}}Nu_z$ and $Re_z^{-\frac{1}{2}}Sh_z$.

Bi	N_b	N_t	Λ	n	S_c	L_e	κ^2	$-Re_z^{\frac{1}{2}}C_f$	$Re_z^{-\frac{1}{2}}Nu_z$	$Re_z^{-\frac{1}{2}}Sh_z$
0.1	0.01	0.03	0.1	1	0.1	0.63		2.352 924	0.998 717	0.272 377
0.2								2.334 257	0.919 071	0.501 312
0.3								2.318 446	0.851 420	0.696 617
0.2	0.01							2.334 257	0.919 071	0.501 312
	0.03							2.345 408	0.918 835	0.167 061
	0.05							2.347 640	0.918 787	0.167 061
	0.01	0.01						2.345 408	0.918 835	0.167 061
		0.03						2.334 257	0.919 071	0.501 312
		0.05						2.323 118	0.919 306	0.835 733
		0.03	0.1					2.334 257	0.919 071	0.501 312
			0.5					2.334 165	0.918 980	0.501 262
			1					2.333 984	0.918 864	0.501 198
			0.1	0				2.311 437	0.829 240	0.452 313
				0.5				2.326 252	0.887 140	0.483 894
				1				2.334 257	0.919 071	0.501 312
				1	1			2.351 416	0.918 558	0.501 031
					2			2.352 731	0.918 499	0.500 999
					3			2.353 190	0.918 472	0.500 985
					0.1	1		2.333 351	0.919 096	0.501 325
						2		2.332 322	0.919 125	0.501 341
						3		2.332 117	0.919 131	0.501 344
						0.63	1	2.314 515	0.919 618	0.501 610
							3	2.328 357	0.919 236	0.501 401
							5	2.334 257	0.919 071	0.501 312

The boundary conditions are given as

$$
\begin{aligned}
\eta = 0: \quad & f'(0) = 1 + \zeta\left(1 + \frac{1}{\beta}\right) f''(0), \quad f(0) = -f_w, \\
& h(0) = 0, \quad h''(0) = 0, \\
& \theta'(0) = -Bi\,(1 - \theta(0)), \\
& N_b\varphi'(0) + N_t\theta'(0) = 0, \\
\eta \to \infty: \quad & f'(\eta) \to 0, \quad h'(\eta) \to 1, \\
& \theta(\eta) \to 0, \quad \varphi(\eta) \to 0,
\end{aligned}
\tag{14}
$$

where $N_r = \dfrac{(\rho_p - \rho_f)}{\rho_f(1-\phi_\infty)\beta_T(T_w - T_\infty)}$ is the buoyancy ratio, $Ri = (1-\phi_\infty)\beta_T(T_w - T_\infty)\dfrac{gz}{U_w^2}$ is the modified local Richardson number, $A = \dfrac{l\lambda}{U}$ is the transient (unsteadiness) parameter, $A_t = \dfrac{\lambda a}{U|1-\lambda t|}$ is the local transient (unsteadiness) parameter with the constant $l = a$, $Q = \dfrac{B_0^2}{\rho\mu_m U^2}$ is the Chandrasekhar number, $\Lambda = \dfrac{(1-\lambda t)\mu_m}{lU}$ is the local inverse modified magnetic Prandtl number, $\gamma = \dfrac{1}{a}\sqrt{\frac{\nu z}{U_w}}$ is the curvature parameter, $Ec = \dfrac{U_w^2}{C_f \Delta T}$ is the Eckert number, $Pr = \dfrac{\nu}{\alpha_f}$ is the (Thermal) Prandtl number, α_f is the thermal diffusivity, $R_d = \dfrac{16\sigma^*}{3k_f k^*}T_\infty^3$ is the Rosseland radiation parameter, $N_b = \tau_0\dfrac{D_B\Delta\phi}{\nu}$, $N_t = \tau_0\dfrac{D_T\Delta T}{\nu T_\infty}$ are the Brownian and thermophoretic parameters, $Le = \dfrac{\alpha_f}{D_B}$ is the modified Lewis number, $\kappa^2 = \dfrac{z\kappa_r}{U_w}(\Delta\phi)^{m-1}$ is the chemical reaction parameter of the nanofluid, $\zeta = N\sqrt{\dfrac{U_w}{\nu U_w}}$ is the slip parameter, $f_w = V_w\sqrt{\dfrac{z}{\nu U_w}}$ is the surface mass flux (suction/injection) at the wall surface. $\Omega = \dfrac{U_e}{U}$ is the velocity ratio of the free stream.

The boundary conditions in equation (14) represent the physical constraints imposed at the surface of the inclined permeable cylinder and in the free stream. At the cylinder surface ($\eta = 0$), the condition ($f(0) = -f_w$) specifies the wall transpiration, where ($f_w > 0$) corresponds to suction and ($f_w < 0$) represents injection. Suction removes fluid from the boundary layer, suppressing momentum, thermal, and concentration boundary-layer growth, whereas injection introduces additional fluid into the flow and generally thickens these layers. The velocity-slip condition $f'(0) = 1 + \zeta\left(1 + \frac{1}{\beta}\right)f''(0)$ accounts for partial slip between the fluid and the wall, which is particularly relevant in microfluidic devices, rarefied gas flows, and nano-engineered surfaces where the classical no-slip assumption is no longer valid.

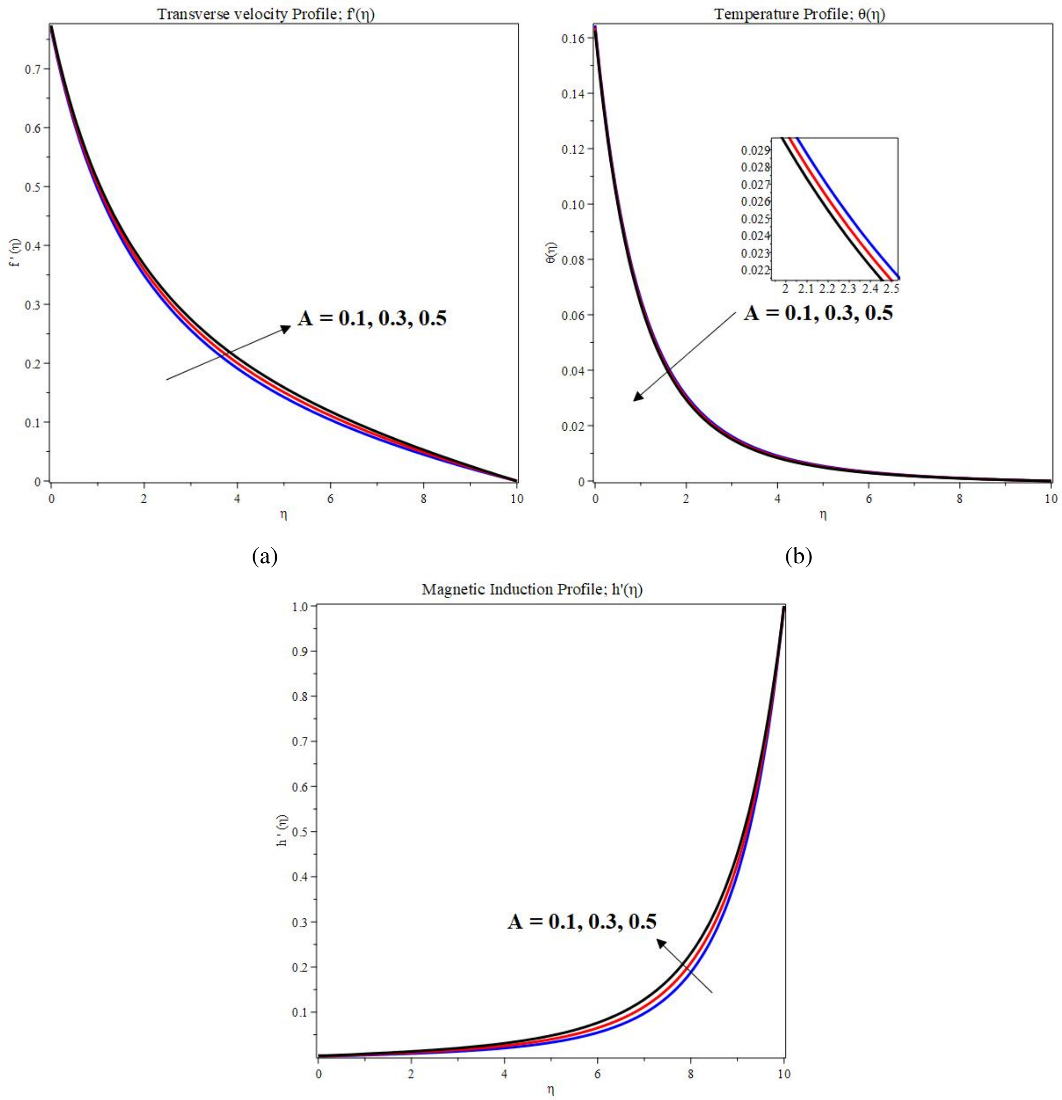

(a) (b)

(c)

Figure 2: Effect of A_t on the velocity, temperature, and magnetic-field profiles

The magnetic boundary conditions ($h(0) = 0$) and ($h''(0) = 0$) ensure compatibility of the induced magnetic field with the impermeable conducting surface and guarantee a physically realistic magnetic field distribution near the wall. The convective thermal boundary condition $\theta'(0) = -Bi(1 - \theta(0))$ models heat exchange between the cylinder and an external heating medium through the Biot number, thereby representing practical situations encountered in cooling and heating systems where the wall temperature is not prescribed but depends on the surrounding environment. Furthermore, the zero nanoparticle mass-flux condition, $[N_b\phi'(0) + N_t\theta'(0) = 0]$ is based on Buongiorno's nanofluid model and implies that there is no net nanoparticle flux across the solid surface. This condition reflects the balance between Brownian diffusion and thermophoretic migration and is widely adopted in nanofluid transport studies involving impermeable walls.

As the similarity variable approaches infinity ($\eta \to \infty$), the conditions ($f'(\eta) \to 0$), ($h'(\eta) \to 1$), ($\theta(\eta) \to 0$), and ($\phi(\eta) \to 0$) indicate that the influence of the cylinder gradually vanishes and the fluid approaches the ambient state. Physically, these conditions ensure that the velocity disturbance, induced magnetic field, excess temperature, and nanoparticle concentration decay smoothly away from the surface, thereby satisfying the far-field equilibrium requirements of the boundary-layer approximation.

2.1. Parameters of engineering interest

The important physical quantities of interest are the local skin friction coefficient C_f, the local Nusselt number Nu_z, and the local Sherwood number NSh_z are defined as

$$C_f = \frac{\tau_w}{\rho_f U_w^2}, \; Nu_z = \frac{z q_w}{k_f \Delta T}, \text{ and } NSh_z = \frac{z j_w}{D_B \Delta\phi}, \qquad (15)$$

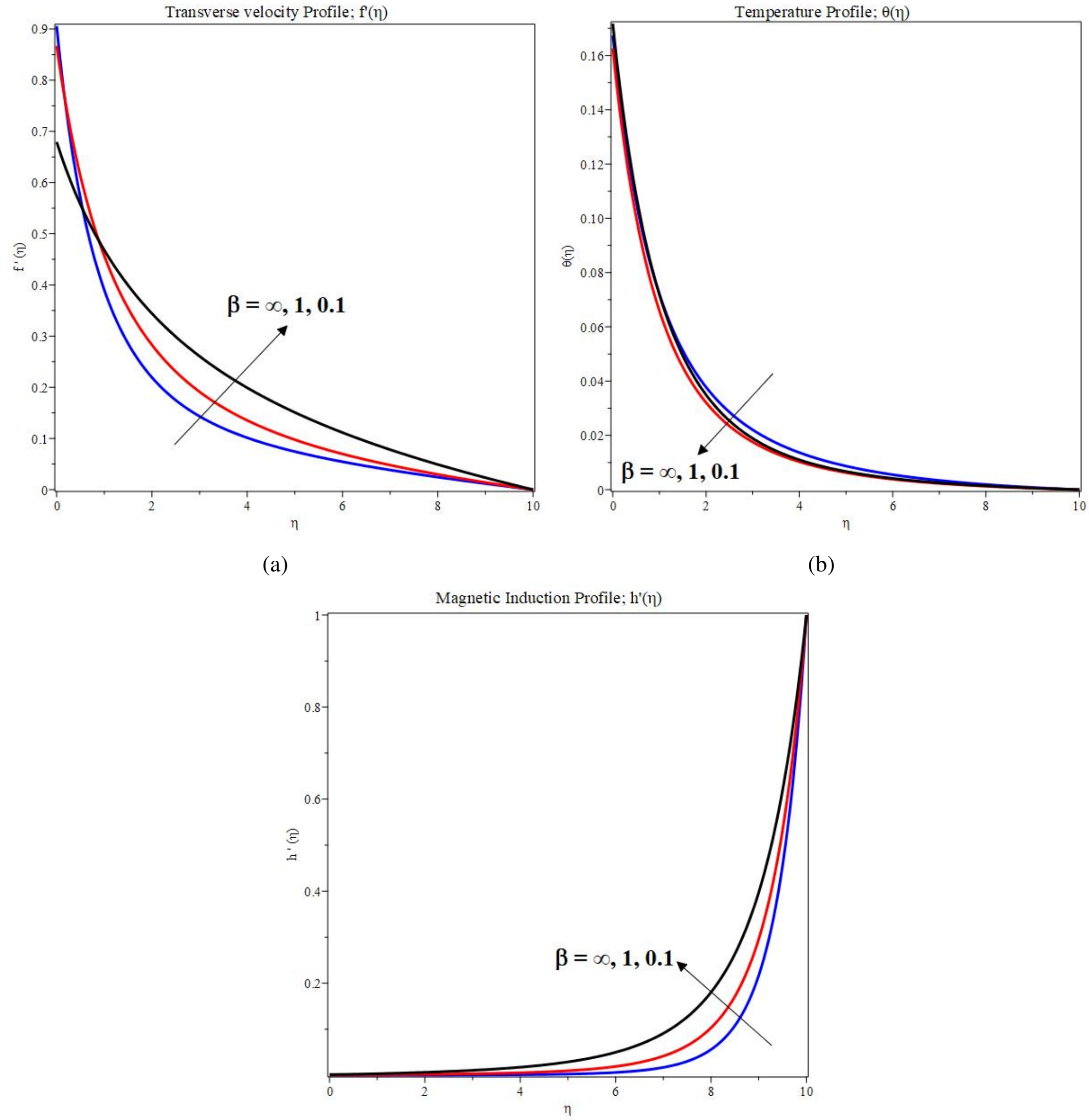

(a) (b) (c)

Figure 3: Effect of β on the velocity, temperature, and magnetic-field profiles

where τ_w is the skin friction or the shear stress along the stretching surface and q_w is the wall heat flux which incorporate the impact of thermal radiation and j_w is the nanofluid volume fraction (flux) transfer at the wall of the cylinder are given respectively as

$$\begin{cases} \tau_w = \mu\left(1+\dfrac{1}{\beta}\right)\left(\dfrac{\partial u}{\partial r}\right)_{r=0}, \\ q_w = \dfrac{z}{\Delta T}k_f\left(1+\dfrac{16\sigma^* T_\infty^3}{3k_f k^*}\right)\left(\dfrac{\partial T}{\partial r}\right)_{r=0}, \\ j_w = D_B\left(\dfrac{\partial \phi}{\partial r}\right)_{r=0}. \end{cases} \tag{16}$$

Substituting the non-dimensionless parameters, we obtain

$$\begin{cases} Re_z^{\frac{1}{2}} C_f = \left(1+\dfrac{1}{\beta}\right) f''(0), \\ Re_z^{-\frac{1}{2}} Nu_z = (1+R_d)\theta'(0), \\ Re_z^{-\frac{1}{2}} NSh_z = \vartheta'(0), \end{cases} \tag{17}$$

where $Re_z = \frac{U_w z}{\nu}$ is the local Reynolds number.

3. Solution method

The transformed governing equations obtained in the previous section constitute a coupled system of nonlinear ordinary differential equations subject to boundary conditions at the wall

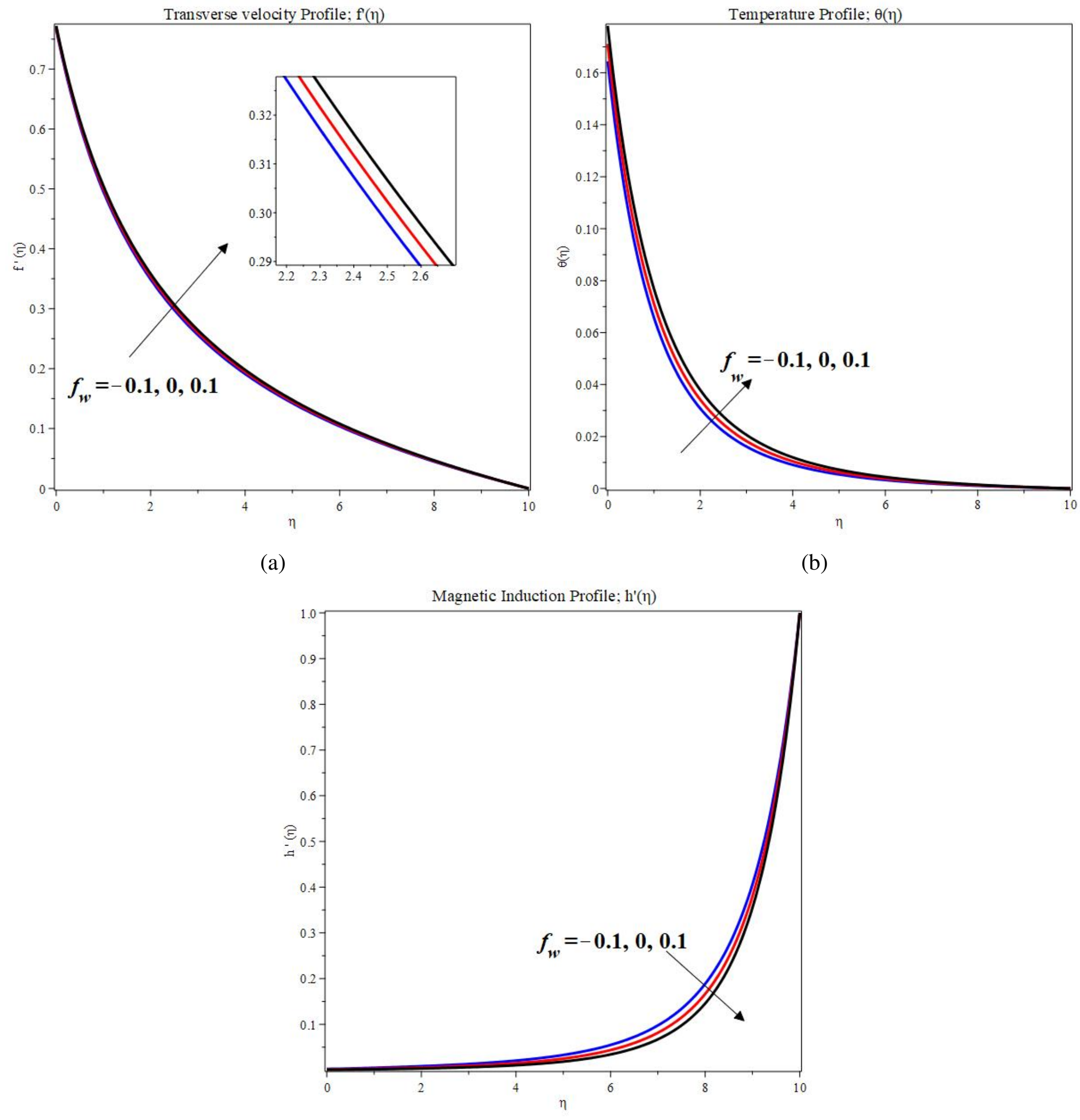

Figure 4: Effect of f_w on the velocity, temperature, and magnetic-field profiles

and at infinity. Because of the nonlinear nature of these equations, obtaining closed-form analytical solutions is generally difficult. Therefore, approximate analytical or numerical techniques are often employed to determine the velocity, temperature, concentration, and magnetic field distributions.

Several approaches have been used in the literature to solve nonlinear boundary-layer equations. Early analytical techniques such as the perturbation method were widely used, but their applicability is often limited to problems involving small parameters. To overcome these limitations, various semi-analytical methods have been developed, including the Adomian decomposition method (ADM), the homotopy analysis method (HAM), and the homotopy perturbation method (HPM). These approaches are capable of handling strongly nonlinear differential equations without requiring linearization or discretization.

The homotopy perturbation method, originally introduced by He, combines the classical perturbation technique with the concept of homotopy from topology to construct rapidly convergent series solutions for nonlinear differential equations. In contrast to classical perturbation techniques, the homotopy perturbation method does not require the existence of a small physical parameter, which makes it particularly suitable for nonlinear boundary-layer flow problems. Over the years, this method has been successfully applied to various nonlinear fluid-flow problems including magnetohydrodynamic flows, nanofluid transport, and heat transfer systems.

Recent studies have further demonstrated the effectiveness of semi-analytical techniques for solving nonlinear transport equations arising in fluid mechanics. For example, Ref. [31]

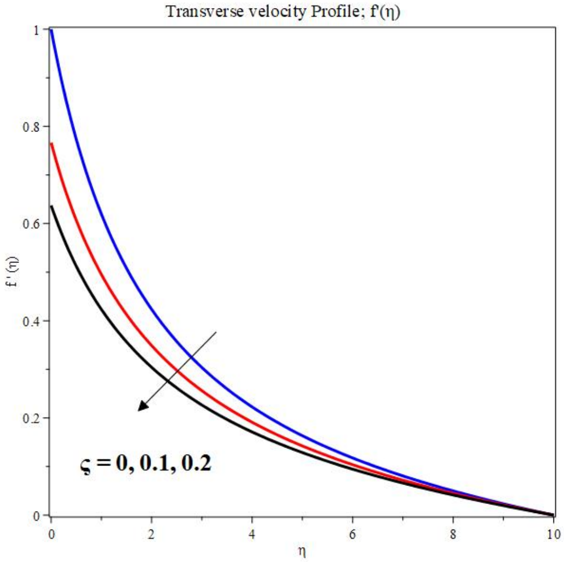

(a)

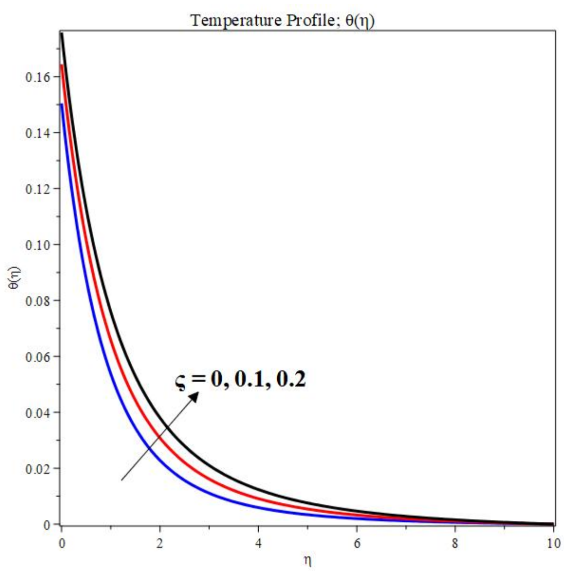

(b)

Figure 5: Effect of slip parameter ς on velocity and temperature profiles.

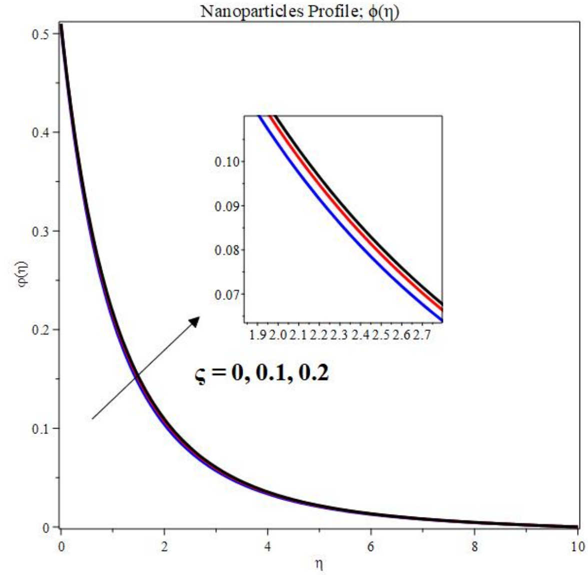

(a)

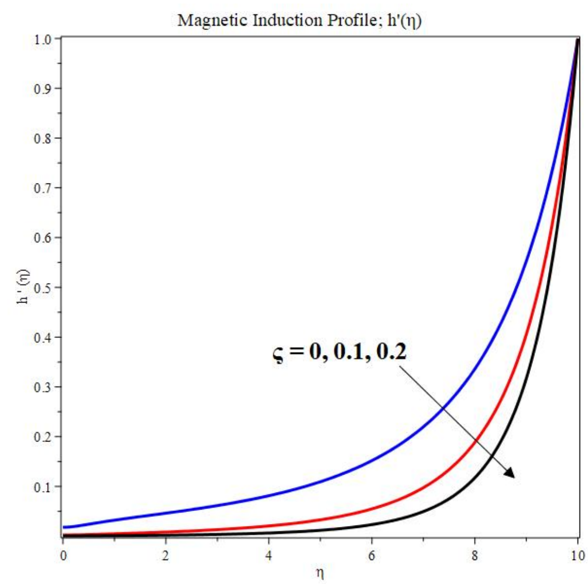

(b)

Figure 6: Effect of the slip parameter ς on the nanoparticle-concentration and magnetic-field profiles.

applied the homotopy perturbation method to investigate viscous dissipation effects in natural convection Couette flow and reported excellent agreement between HPM results and numerical solutions obtained using Runge–Kutta methods.

Similarly, Ref. [32] employed a modified homotopy perturbation method to analyze magnetohydrodynamic Jeffery–Hamel nanofluid flow and demonstrated that the method provides accurate approximations for velocity and shear stress profiles under different physical conditions.

Other recent investigations have also used semi-analytical techniques such as optimal homotopy perturbation and homotopy analysis methods to examine nonlinear nanofluid transport problems involving magnetic fields and porous media. These studies showed that such methods offer rapid convergence and reliable solutions for nonlinear boundary value problems arising in magnetohydrodynamic flows.

Motivated by these advantages, the present study employs a semi-analytical homotopy perturbation method to obtain approximate analytical solutions for the transformed nonlinear system of equations governing the Casson nanofluid flow.

3.1. Semi-analytic method

To apply the homotopy perturbation method, the nonlinear differential equations governing the flow, temperature, nanoparticle concentration, and magnetic field are first expressed in operator form as

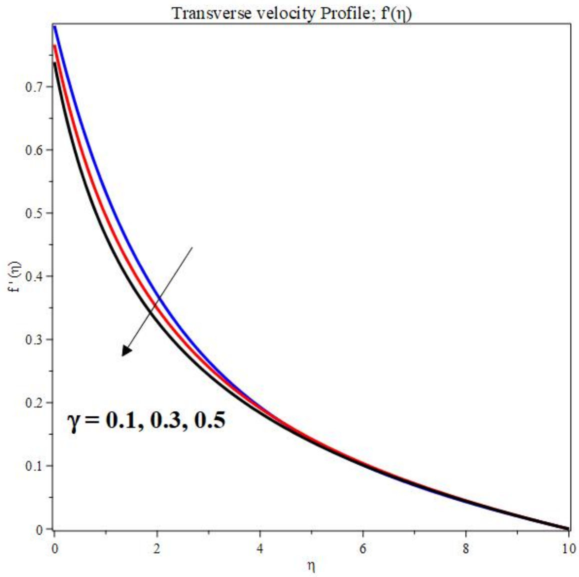

(a)

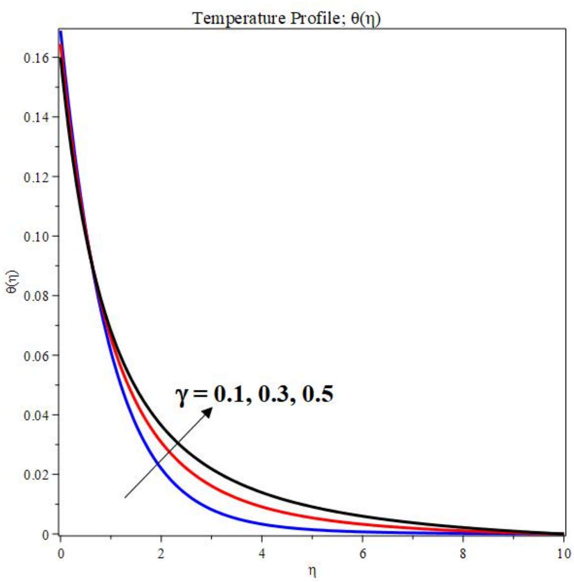

(b)

Figure 7: Effect of curvature parameter γ on velocity and temperature profiles.

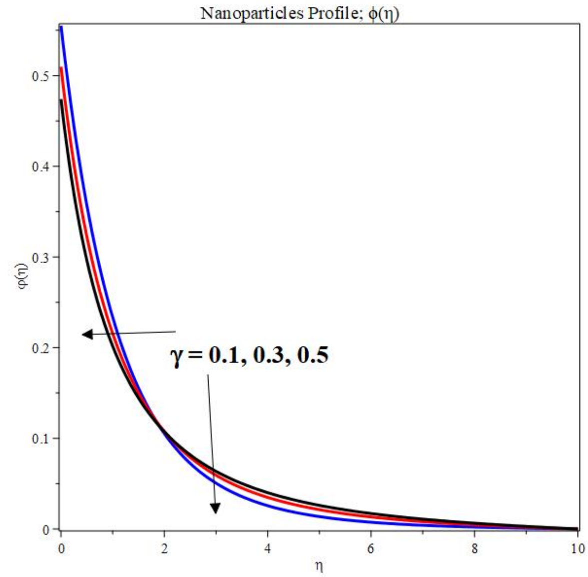

(a)

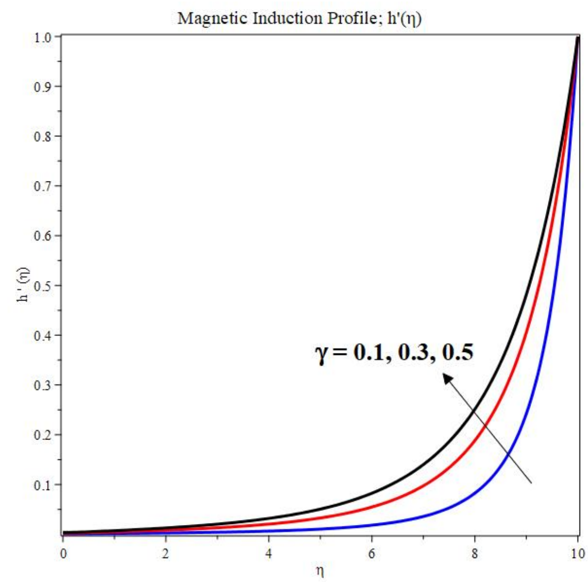

(b)

Figure 8: Effect of the curvature parameter γ on the nanoparticle-concentration and magnetic-field profiles.

$$\mathcal{L}(f) + \mathcal{N}(f) = 0, \tag{18}$$

where $\mathcal{L}$ represents the linear operator and $\mathcal{N}$ denotes the nonlinear operator. The homotopy perturbation method constructs a homotopy $\mathcal{H}(\eta, p)$ defined as

$$\mathcal{H}(\eta, p) = (1-p)\mathcal{L}(f) + p\left[\mathcal{L}(f) + \mathcal{N}(f)\right] = 0, \tag{19}$$

where $p \in [0, 1]$ is an embedding parameter. When $p = 0$, the system reduces to a simpler linear equation whose solution is known. When $p = 1$, the original nonlinear problem is recovered. These will take the forms

$$\begin{aligned}\mathcal{H}_1(\eta, f, \theta, \varphi, h, p) \equiv{}& (1-p)\left(1+\frac{1}{\beta}\right)f''' \\ &+ p\Bigg[\left(1+\frac{1}{\beta}\right)((1+2\gamma\eta)f''' + 2\gamma f'') \\ &\quad + ff'' - (f')^2 + Ri(\theta - N_r\varphi) \\ &\quad - \Gamma Da\left(1+\frac{1}{\beta}\right)(f' - \Omega) \\ &\quad + QZ^2\left((h')^2 - hh'' - 1\right) + A\Omega + \Omega^2\Bigg] = 0.\end{aligned} \tag{20}$$

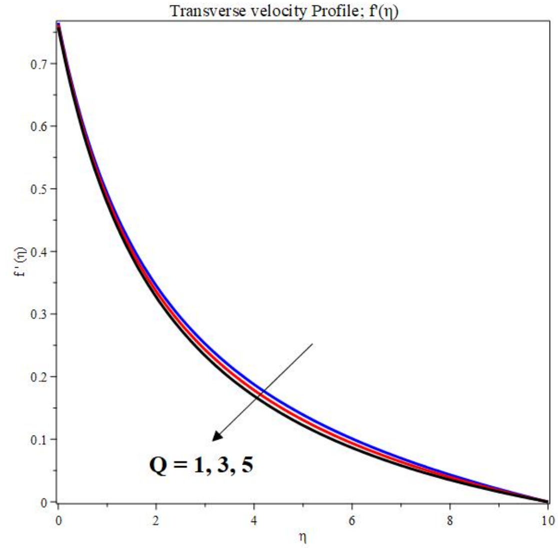

(a)

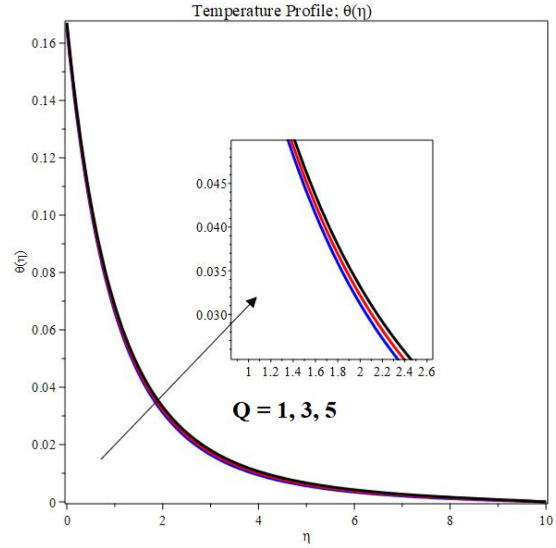

(b)

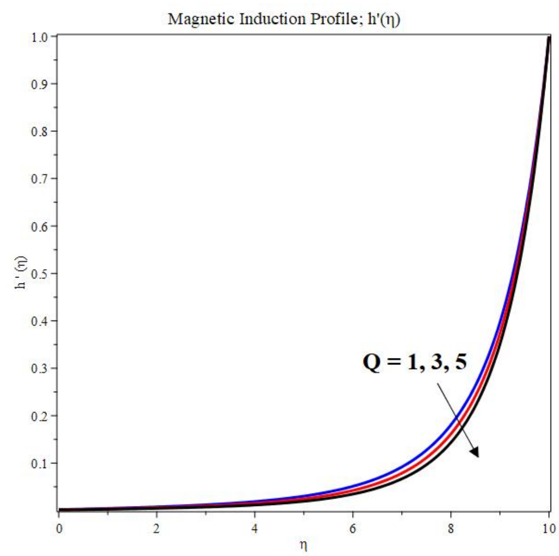

(c)

Figure 9: Effect of the Chandrasekhar number Q on the velocity, temperature, and magnetic-field profiles.

$$
\begin{aligned}
\mathcal{H}_2(\eta, f, \theta, \varphi, h, p) \equiv{}& (1-p)\,\frac{1+R_d}{Pr}\,\theta'' \\
&+ p\Bigg[\frac{1+R_d}{Pr}\left((1+2\gamma\eta)\theta'' + 2\gamma\theta'\right) \\
&\quad + Ec\left(1+\frac{1}{\beta}\right)(1+2\gamma\eta)(f'')^2 \\
&\quad + f\theta' - nf'\theta + G\theta^{\varpi} \\
&\quad + (1+2\gamma\eta)\left(N_b\varphi'\theta' + N_t(\theta')^2\right) \\
&\quad + Q\Lambda Ec(h'')^2\Bigg] = 0.
\end{aligned}
\tag{21}
$$

$$
\begin{aligned}
\mathcal{H}_3(\eta, f, \theta, \varphi, h, p) \equiv{}& (1-p)\,\frac{1}{Sc}\,\varphi'' \\
&+ p\Bigg[\frac{1}{Sc}\left((1+2\gamma\eta)\varphi'' + 2\gamma\varphi'\right) \\
&\quad + f\varphi' - nf'\varphi \\
&\quad + \frac{1}{Le\,Pr}\,\frac{N_t}{N_b}\left((1+2\gamma\eta)\theta'' + 2\gamma\theta'\right) \\
&\quad - \kappa^2\varphi^m\Bigg] = 0.
\end{aligned}
\tag{22}
$$

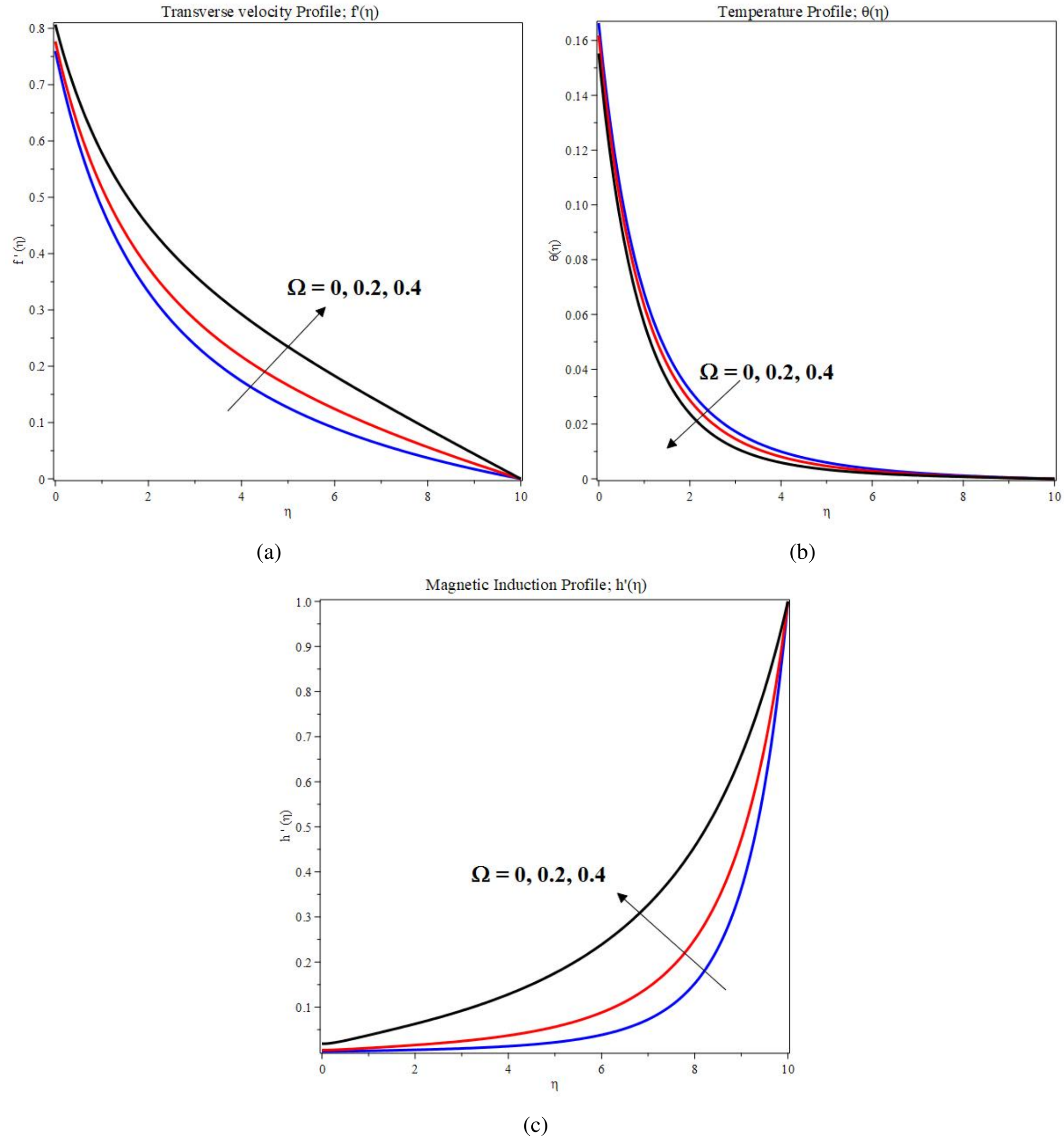

Figure 10: Effect of the velocity ratio Ω on the velocity, temperature, and magnetic-field profiles.

$$\mathcal{H}_4(\eta, f, \theta, \varphi, h, p) \equiv (1-p)\,\Lambda\, h''' + p\Big[\Lambda\left((1+2\gamma\eta)h''' + 2\gamma h''\right) + fh'' - hf'' - A_t\left(h' + \tfrac{1}{2}\eta h''\right)\Big] = 0. \tag{23}$$

The solution is then expressed as a power series in terms of the embedding parameter

$$f(\eta) = f_0(\eta) + pf_1(\eta) + p^2 f_2(\eta) + \cdots . \tag{24}$$

Similarly, the temperature, concentration, and magnetic field functions can be written as

$$\theta(\eta) = \theta_0 + p\theta_1 + p^2\theta_2 + \cdots \tag{25}$$

$$\phi(\eta) = \phi_0 + p\phi_1 + p^2\phi_2 + \cdots \tag{26}$$

$$h(\eta) = h_0 + ph_1 + p^2 h_2 + \cdots . \tag{27}$$

Substituting these series expansions into the governing equations and equating the coefficients of identical powers of p produces a sequence of linear differential equations that can be solved successively. The resulting series solutions converge rapidly to the approximate analytical solutions of the original nonlinear boundary value problem.

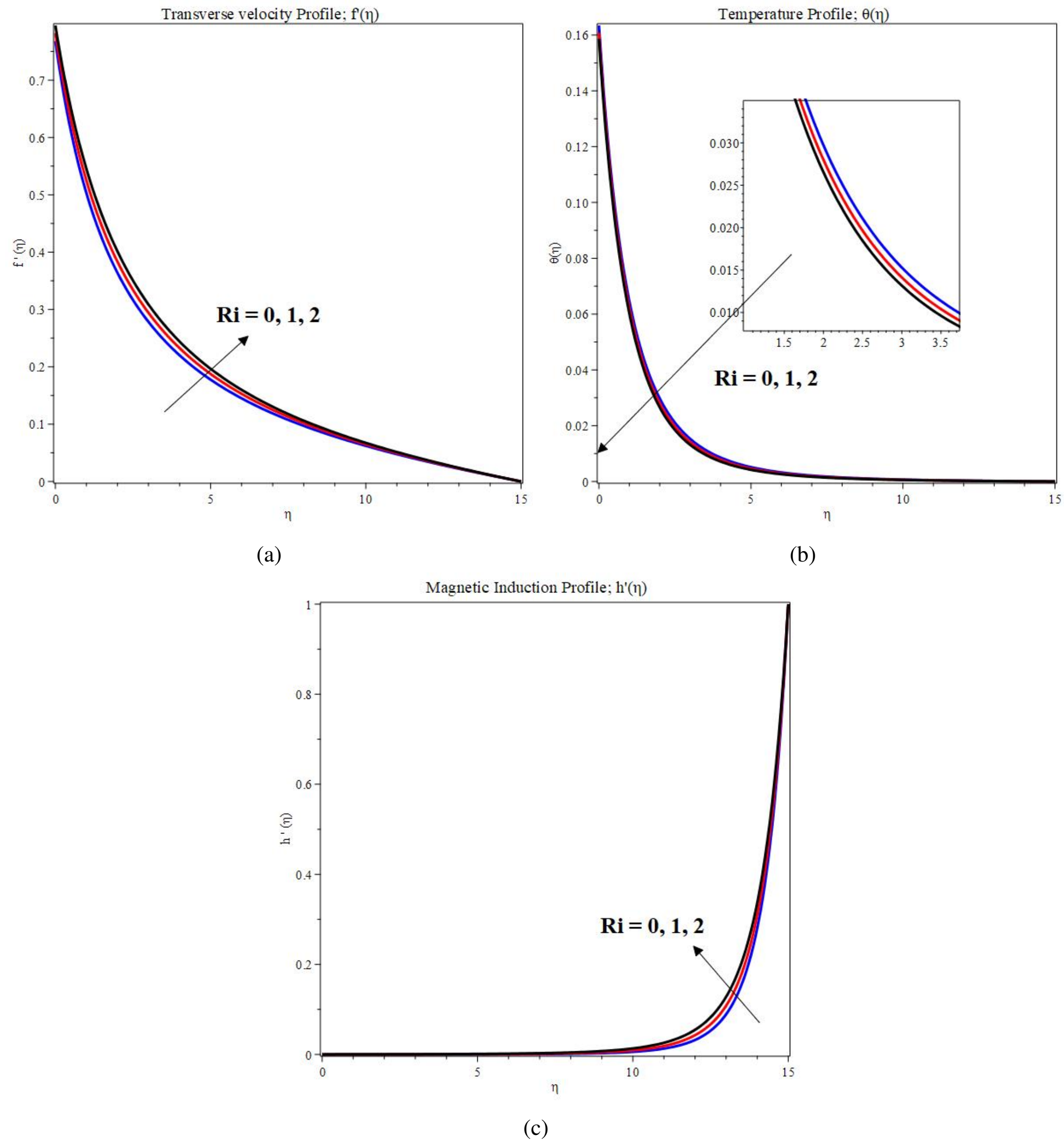

Figure 11: Effect of the Richardson number Ri on the velocity, temperature, and magnetic-field profiles.

$$
\begin{aligned}
&(1-p)\left(1+\frac{1}{\beta}\right)\left(f_0''' + pf_1''' + p^2 f_2''' + \cdots\right)\\
&\quad + p\Bigg[\left(1+\frac{1}{\beta}\right)\Big((1+2\gamma\eta)(f_0''' + pf_1''' + \cdots) + 2\gamma(f_0'' + pf_1'' + \cdots)\Big)\\
&\qquad + (f_0 + pf_1 + \cdots)(f_0'' + pf_1'' + \cdots) - (f_0' + pf_1' + \cdots)^2\\
&\qquad + Ri\Big((\theta_0 + p\theta_1 + \cdots) - N_r(\varphi_0 + p\varphi_1 + \cdots)\Big) + A\Omega + \Omega^2\\
&\qquad - \Lambda Da\left(1+\frac{1}{\beta}\right)(f_0' + pf_1' + \cdots - \Omega)\\
&\qquad - QZ^2 + QZ^2(h_0' + ph_1' + \cdots)\\
&\qquad - (h_0 + ph_1 + \cdots)(h_0'' + ph_1'' + \cdots)\Bigg] = 0.
\end{aligned} \tag{28}
$$

$$
\begin{aligned}
&(1-p)\frac{1+R_d}{Pr}\left(\theta_0'' + p\theta_1'' + p^2\theta_2'' + \cdots\right)\\
&\quad + p\Bigg[\frac{1+R_d}{Pr}\Big((1+2\gamma\eta)(\theta_0'' + p\theta_1'' + \cdots) + 2\gamma(\theta_0' + p\theta_1' + \cdots)\Big)\\
&\qquad + Ec\left(1+\frac{1}{\beta}\right)(1+2\gamma\eta)\left(f_0'' + pf_1'' + \cdots\right)^2\\
&\qquad + G\left(\theta_0 + p\theta_1 + \cdots\right)^{\varpi} + (f_0 + pf_1 + \cdots)(\theta_0' + p\theta_1' + \cdots)\\
&\qquad - n(f_0' + pf_1' + \cdots)(\theta_0 + p\theta_1 + \cdots)\\
&\qquad + (1+2\gamma\eta)\Big[N_b(\varphi_0' + p\varphi_1' + \cdots)(\theta_0' + p\theta_1' + \cdots)\\
&\qquad + N_t(\theta_0' + p\theta_1' + \cdots)^2\Big] + Q\Lambda Ec\left(h_0'' + ph_1'' + \cdots\right)^2\Bigg] = 0.
\end{aligned} \tag{29}
$$

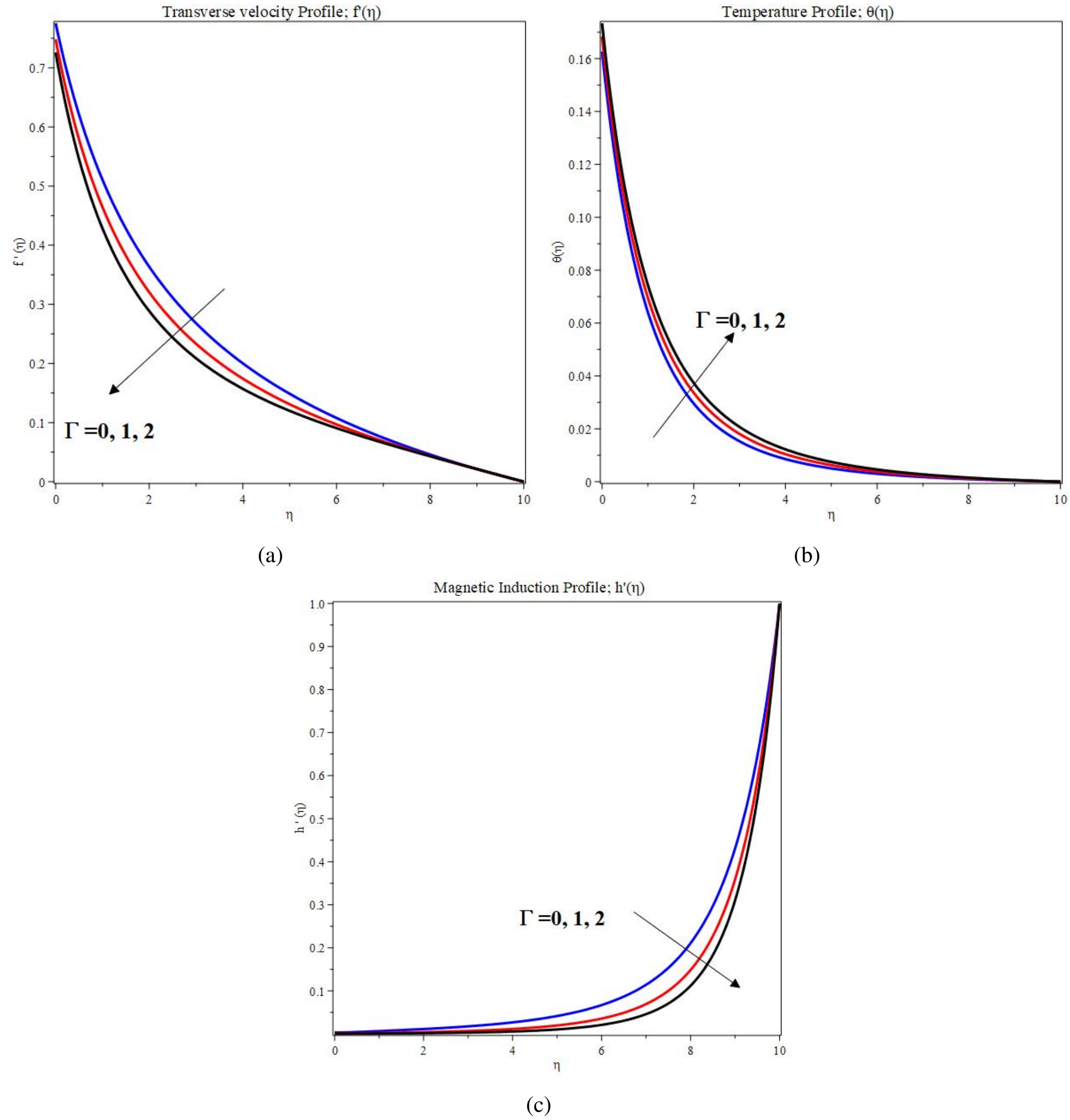

Figure 12: Effect of the anisotropic porous-medium parameter Γ on the velocity, temperature, and magnetic-field profiles.

$$
\begin{aligned}
&(1-p)\frac{1}{Sc}\left(\varphi_0'' + p\varphi_1'' + p^2\varphi_2'' + \cdots\right)\\
&\quad + p\Bigg[\frac{1}{Sc}\Big((1+2\gamma\eta)(\varphi_0'' + p\varphi_1'' + \cdots) + 2\gamma(\varphi_0' + p\varphi_1' + \cdots)\Big)\\
&\qquad + (f_0 + pf_1 + \cdots)(\varphi_0' + p\varphi_1' + \cdots)\\
&\qquad - n(f_0' + pf_1' + \cdots)(\varphi_0 + p\varphi_1 + \cdots)\\
&\qquad + \frac{1}{Le\,Pr}\frac{N_t}{N_b}\Big((1+2\gamma\eta)(\theta_0'' + p\theta_1'' + \cdots) + 2\gamma(\theta_0' + p\theta_1' + \cdots)\Big)\\
&\qquad - \kappa^2(\varphi_0 + p\varphi_1 + \cdots)^m\Bigg] = 0.
\end{aligned} \tag{30}
$$

$$
\begin{aligned}
&(1-p)\,\Lambda\left(h_0''' + ph_1''' + p^2h_2''' + \cdots\right)\\
&\quad + p\Bigg[\Lambda\Big((1+2\gamma\eta)(h_0''' + ph_1''' + \cdots) + 2\gamma(h_0'' + ph_1'' + \cdots)\Big)\\
&\qquad + (f_0 + pf_1 + \cdots)(h_0'' + ph_1'' + \cdots)\\
&\qquad - (h_0 + ph_1 + \cdots)(f_0'' + pf_1'' + \cdots)\\
&\qquad - A_t\Big((h_0' + ph_1' + \cdots) + \tfrac{1}{2}\eta(h_0'' + ph_1'' + \cdots)\Big)\Bigg] = 0.
\end{aligned} \tag{31}
$$

Also, the boundary conditions in equation (14), we have

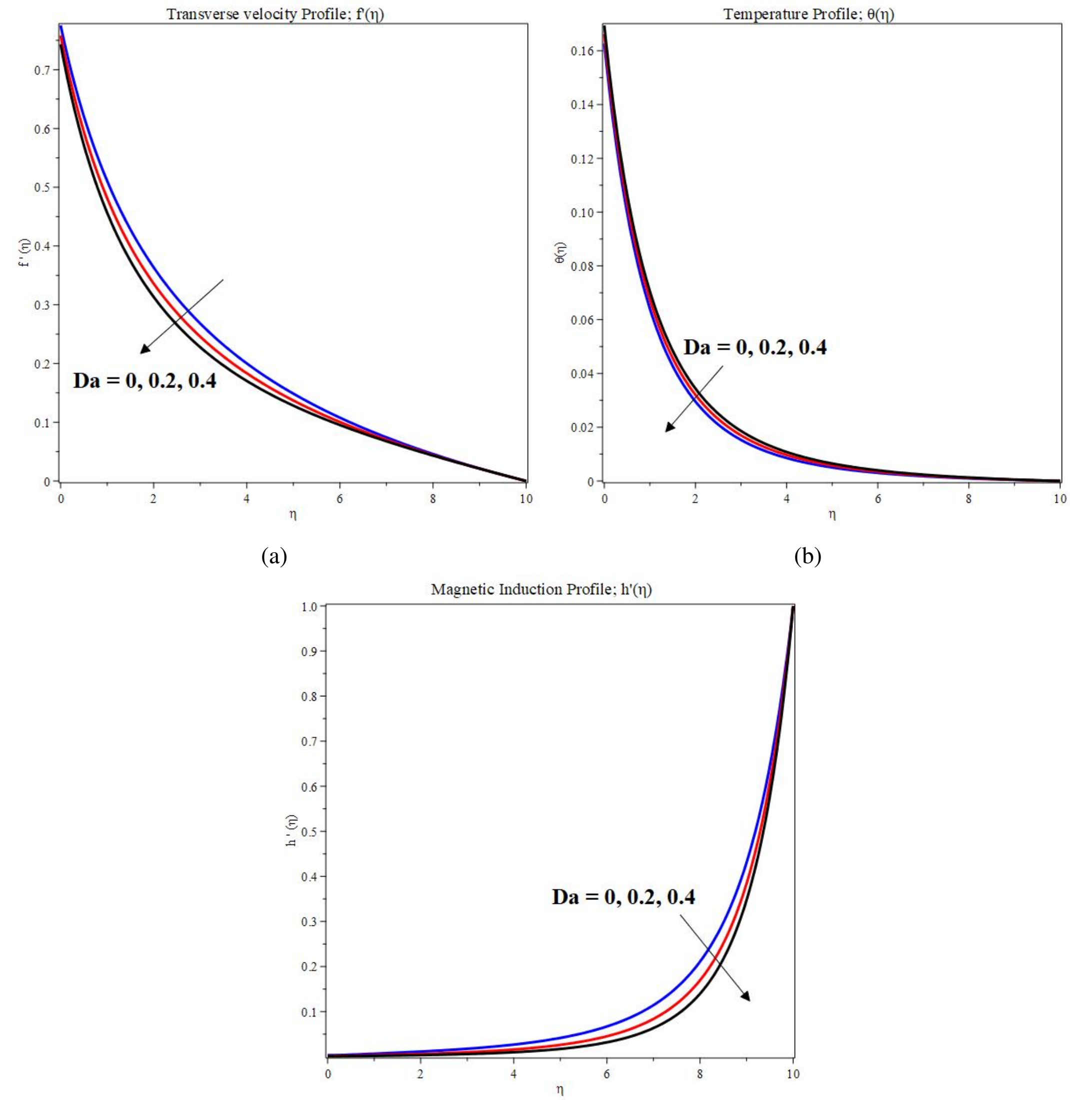

(a) (b)

(c)

Figure 13: Effect of the Darcy number Da on the velocity, temperature, and magnetic-field profiles.

$$\eta = 0: \quad f_0(0) + pf_1(0) + p^2 f_2(0) + \cdots = -f_w, \tag{32a}$$

$$f_0'(0) + pf_1'(0) + p^2 f_2'(0) + \cdots = 1 + \zeta\left(1 + \frac{1}{\beta}\right)(f_0''(0) + pf_1''(0) + \cdots), \tag{32b}$$

$$h_0(0) + ph_1(0) + p^2 h_2(0) + \cdots = 0, \tag{32c}$$

$$h_0''(0) + ph_1''(0) + p^2 h_2''(0) + \cdots = 0, \tag{32d}$$

$$\theta_0'(0) + p\theta_1'(0) + p^2\theta_2'(0) + \cdots = -Bi\,[1 - (\theta_0(0) + p\theta_1(0) + \cdots)], \tag{32e}$$

$$N_b\,(\varphi_0'(0) + p\varphi_1'(0) + \cdots) + N_t\,(\theta_0'(0) + p\theta_1'(0) + \cdots) = 0, \tag{32f}$$

$$\eta \to \infty: \quad f_0'(\infty) + pf_1'(\infty) + p^2 f_2'(\infty) + \cdots = 0, \tag{32g}$$

$$h_0'(\infty) + ph_1'(\infty) + p^2 h_2'(\infty) + \cdots = 1, \tag{32h}$$

$$\theta_0(\infty) + p\theta_1(\infty) + p^2\theta_2(\infty) + \cdots = 0, \tag{32i}$$

$$\varphi_0(\infty) + p\varphi_1(\infty) + p^2\varphi_2(\infty) + \cdots = 0. \tag{32j}$$

To be able to arrange the equations above and their boundary conditions according to the powers of the embedding parameter p, we need to specify the value(s) of $n(= 0, 1, 2, 3)$. Then, we have

$$p^{(0)}: \quad \left(1 + \frac{1}{\beta}\right) f_0''' = 0, \qquad \frac{1 + R_d}{Pr}\theta_0'' = 0, \qquad \frac{1}{Sc}\varphi_0'' = 0, \qquad \Lambda h_0''' = 0, \tag{33a}$$

$$f_0(0) = -f_w, \qquad f_0'(0) = 1 + \zeta\left(1 + \frac{1}{\beta}\right) f_0''(0), \qquad h_0(0) = h_0''(0) = 0, \qquad \theta_0(0) = \varphi_0(0) = 1, \tag{33b}$$

$$f_0'(\infty) = 0, \qquad h_0'(\infty) = 1, \qquad \theta_0(\infty) = \varphi_0(\infty) = 0. \tag{33c}$$

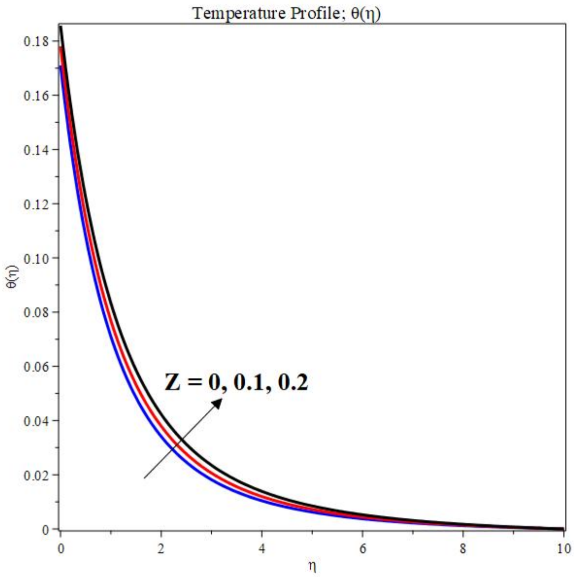

(a)

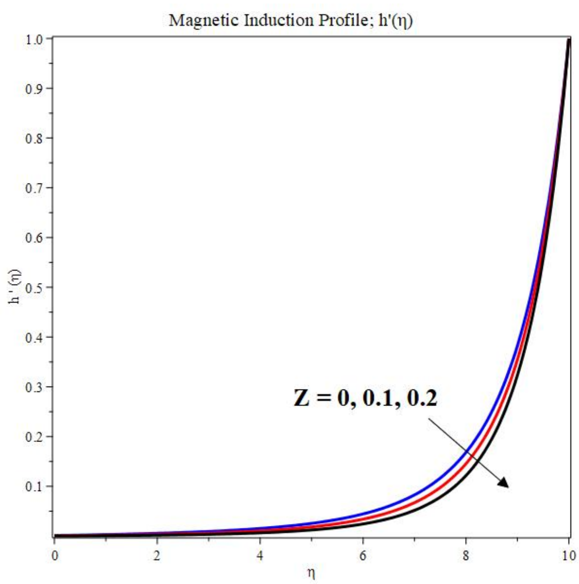

(b)

Figure 14: Effect of scaled axial position Z on temperature and magnetic profiles.

$$
\begin{aligned}
p^1: \quad & \left(1+\frac{1}{\beta}\right)f_1''' + 2\gamma\left(1+\frac{1}{\beta}\right)\eta f_0''' \\
& + 2\gamma\left(1+\frac{1}{\beta}\right)f_0'' + f_0 f_0'' - (f_0')^2 \\
& + Ri(\theta_0 - N_r\varphi_0) - \Lambda Da\left(1+\frac{1}{\beta}\right)(f_0' - \Omega) \\
& + QZ^2\left((h_0')^2 - h_0 h_0'' - 1\right) + A\Omega + \Omega^2 = 0, \qquad (34a) \\
& f_1(0) = 0, \qquad f_1'(0) = \zeta\left(1+\frac{1}{\beta}\right)f_1''(0), \\
& f_1'(\infty) = 0. \qquad (34b)
\end{aligned}
$$

$$
\begin{aligned}
p^1: \quad & \frac{1+R_d}{Pr}\theta_1'' + \frac{2\gamma(1+R_d)}{Pr}\eta\theta_0'' + \frac{2\gamma(1+R_d)}{Pr}\theta_0' \\
& + Ec\left(1+\frac{1}{\beta}\right)(1+2\gamma\eta)(f_0'')^2 \\
& + f_0\theta_0' - nf_0'\theta_0 + G\theta_0^{\varpi} \\
& + (1+2\gamma\eta)\left(N_b\varphi_0'\theta_0' + N_t(\theta_0')^2\right) \\
& + Q\Lambda Ec(h_0'')^2 = 0, \qquad (35a) \\
& \theta_1(0) = 0, \qquad \theta_1(\infty) = 0. \qquad (35b)
\end{aligned}
$$

$$
\begin{aligned}
& \frac{1}{Sc}\varphi_1'' + \frac{2\gamma}{Sc}\eta\varphi_0'' + \frac{2\gamma}{Sc}\varphi_0' \\
& + f_0\varphi_0' - nf_0'\varphi_0 \\
& + \frac{1}{Le\,Pr}\frac{N_t}{N_b}\left((1+2\gamma\eta)\theta_0'' + 2\gamma\theta_0'\right) - \kappa^2\varphi_0 = 0, \qquad (36a) \\
& \varphi_1(0) = 0, \qquad \varphi_1(\infty) = 0. \qquad (36b)
\end{aligned}
$$

$$
\begin{aligned}
& \Lambda h_1''' + 2\gamma\Lambda\eta h_0''' + 2\gamma\Lambda h_0'' f_0 h_0'' \\
& - A_t\left(h_0' + \frac{1}{2}\eta h_0''\right) = 0, \qquad (37a) \\
& h_1(0) = 0, \qquad h_1''(0) = 0, \qquad h_1'(\infty) = 0. \qquad (37b)
\end{aligned}
$$

$$
\begin{aligned}
p^{(2)}: \quad & \left(1+\frac{1}{\beta}\right)f_2''' + \left(1+\frac{1}{\beta}\right)(2\gamma\eta f_1''' + 2\gamma f_1'') \\
& + f_0 f_1'' + f_1 f_0'' - 2f_0' f_1' + Ri(\theta_1 - N_r\varphi_1) \\
& + QZ^2\left(2h_0'h_1' - h_0 h_1'' - h_1 h_0''\right) \\
& - \Gamma Da\left(1+\frac{1}{\beta}\right)f_1' = 0, \qquad (38a) \\
& f_2(0) = 0, \qquad f_2'(0) = \zeta\left(1+\frac{1}{\beta}\right)f_2''(0), \\
& f_2'(\infty) = 0. \qquad (38b)
\end{aligned}
$$

$$
\begin{aligned}
& \frac{1+R_d}{Pr}\theta_2'' + \frac{1+R_d}{Pr}\left(2\gamma\eta\theta_1'' + 2\gamma\theta_1'\right) \\
& + 2Ec\left(1+\frac{1}{\beta}\right)(1+2\gamma\eta)f_0''f_1'' \\
& + f_0\theta_1' + f_1\theta_0' - nf_0'\theta_1 - nf_1'\theta_0 + G\theta_1 \\
& + (1+2\gamma\eta)\left(N_b\varphi_0'\theta_1' + N_b\varphi_1'\theta_0' + 2N_t\theta_0'\theta_1'\right) \\
& + 2Q\Lambda Ec\, h_0''h_1'' = 0, \qquad (39a) \\
& \theta_2(0) = 0, \qquad \theta_2(\infty) = 0. \qquad (39b)
\end{aligned}
$$

$$
\begin{aligned}
& \frac{1}{Sc}\varphi_2'' + \frac{1}{Sc}\left(2\gamma\eta\varphi_1'' + 2\gamma\varphi_1'\right) \\
& + \frac{1}{Pr\,Le}\frac{N_t}{N_b}\left((1+2\gamma\eta)\theta_1'' + 2\gamma\theta_1'\right) \\
& - \kappa^2\varphi_1 + f_0\varphi_1' + f_1\varphi_0' - nf_0'\varphi_1 - nf_1'\varphi_0 = 0, \qquad (40a) \\
& \varphi_2(0) = 0, \qquad \varphi_2(\infty) = 0. \qquad (40b)
\end{aligned}
$$

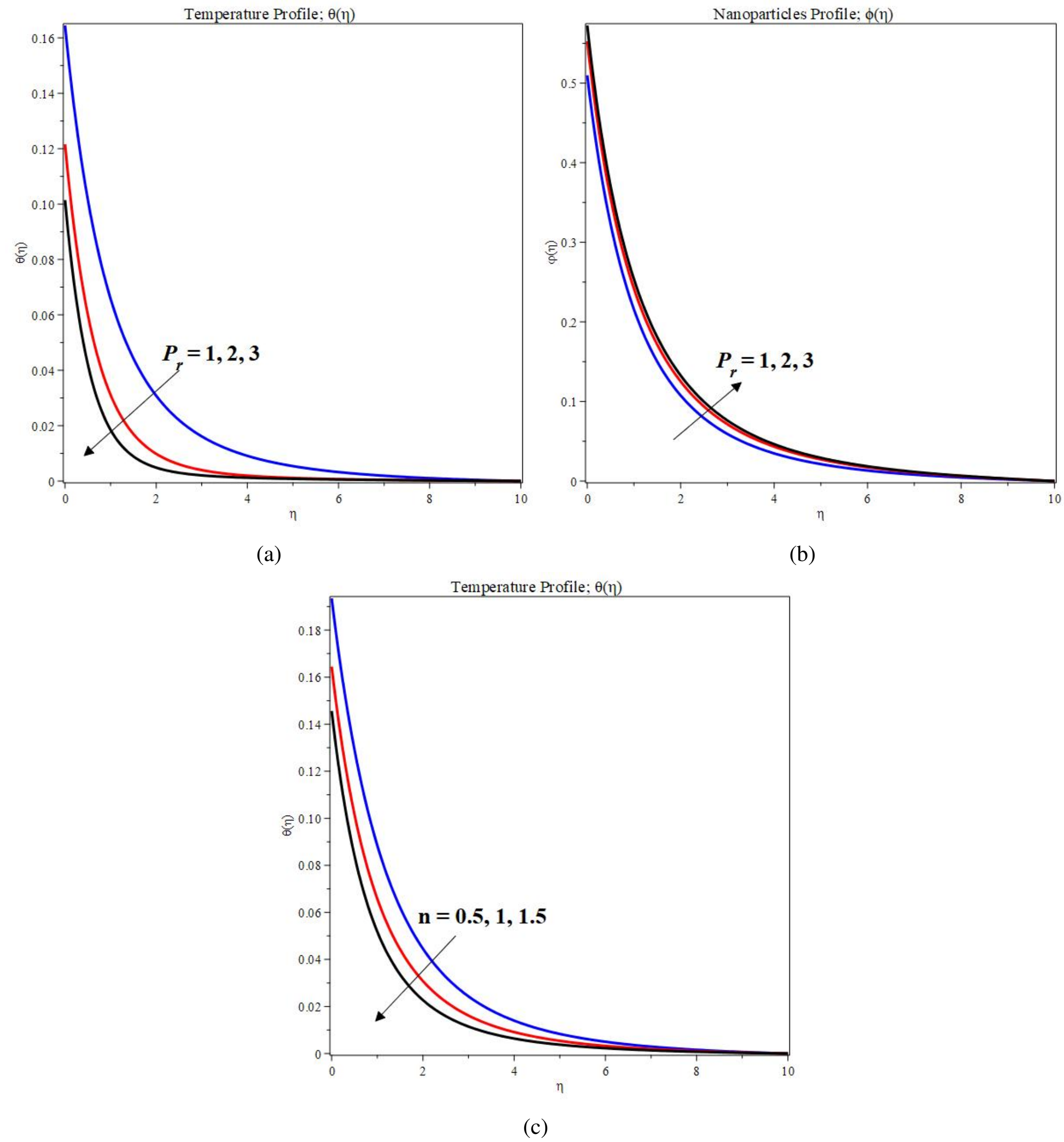

(a) (b) (c)

Figure 15: Effect of the Prandtl number Pr and temperature exponent n on the temperature and nanoparticle-concentration profiles.

$$\Lambda h_2''' + \Lambda\left(2\gamma\eta h_1''' + 2\gamma h_1''\right) - h_0 f_1'' - h_1 f_0'' + f_0 h_1'' + f_1 h_0'' - A_t\left(h_1'' + \frac{1}{2}\eta h_1''\right) = 0, \tag{41a}$$

$$h_2(0) = 0, \qquad h_2''(0) = 0, \qquad h_1'(\infty) = 0. \tag{41b}$$

For ease of convergence and less computation power, we employ some initial solutions for $f_0, \theta_0, \varphi_0,$ and h_0 as

$$f_0 = a_1 + b_1\eta + c_1 e^{-k\eta} \tag{42}$$

$$\theta_0 = a_2 + b_2 e^{-k\eta} \tag{43}$$

$$\varphi_0 = a_3 + b_3 e^{-k\eta} \tag{44}$$

$$h_0 = a_4 + b_4\eta + c_4 e^{-k\eta} \tag{45}$$

where $a_i, b_i,$ and c_i, $i = 1, 2, 3$ are arbitrary constants;

Solving equation (42) conforming with the boundary conditions in equation (33) to obtain

$$\begin{aligned} f_0(\eta) &= -f_w + \frac{1}{k(1+\alpha k)}\left(1 - e^{-k\eta}\right), \\ \theta_0(\eta) &= \frac{Bi}{k+Bi}\, e^{-k\eta}, \\ \varphi_0(\eta) &= -\frac{N_t}{N_b}\,\frac{Bi}{k+Bi}\, e^{-k\eta}, \\ h_0(\eta) &= \eta, \end{aligned} \tag{46}$$

where $\alpha = \zeta\left(1 + \frac{1}{\beta}\right)$.

Equation (46) makes the solutions easy to compute

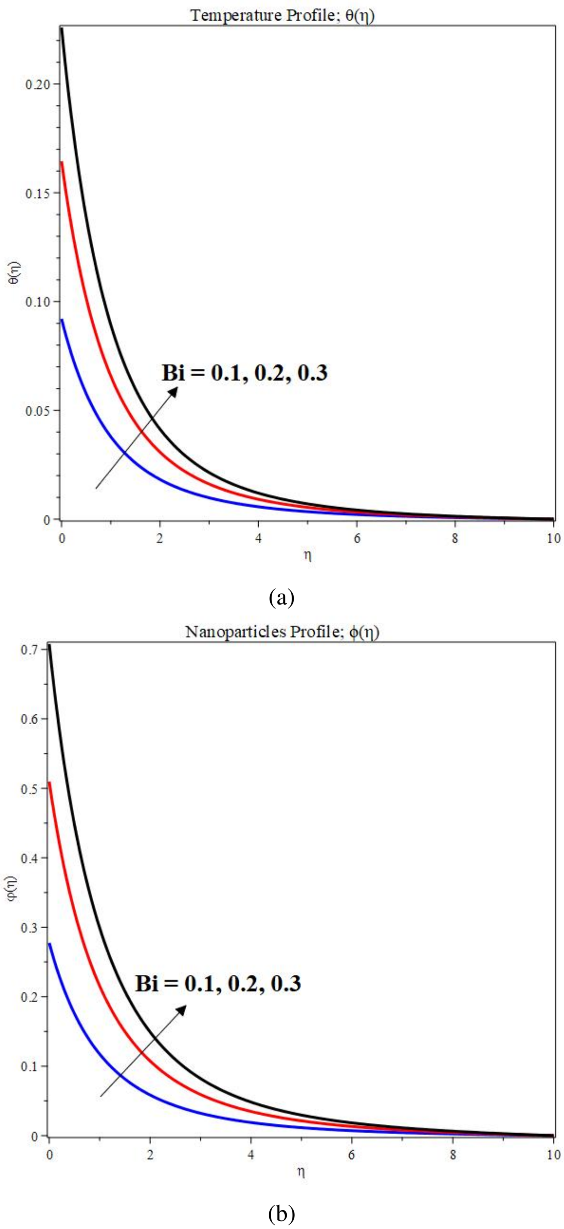

Figure 16: Effect of Biot number Bi on temperature and nanoparticle profiles.

$f_i(\eta), \theta_i(\eta), \varphi_i(\eta)$, and $h_i(\eta)$, $i = 1, 2, \ldots$ analytically and solving them with their respective boundary conditions. Therefore, taking the limit as $p \to 1$ for $f_i(\eta), \theta_i(\eta), \varphi_i(\eta)$, and $h_i(\eta)$, $i = 0, 1, 2, \ldots$ and take the form as in equations (24)–(25), we have

$$f(\eta) = f_0(\eta) + f_1(\eta) + f_2(\eta) + \ldots \tag{47}$$
$$\theta(\eta) = \theta_0(\eta) + \theta_1(\eta) + \theta_2(\eta) + \ldots \tag{48}$$
$$\varphi(\eta) = \varphi_0(\eta) + \varphi_1(\eta) + \varphi_2(\eta) + \ldots \tag{49}$$
$$h(\eta) = h_0(\eta) + h_1(\eta) + h_2(\eta) + \ldots \tag{50}$$

It would be noted from equations (34), (35), (36), and (37) that the first iteration conforms to the governing equations (10), (11), (12), and (13). Thus, the solutions converges for most of the parameters after the first iteration. Although, in some cases we might go higher to second and third iteration depending on the difficulties of the problem. The accuracy of the obtained semi-analytical solutions can be verified by comparing them with previously published results for limiting cases. Such comparisons typically show excellent agreement, confirming the validity of the method.

4. Results and discussion

This section analyzes the effects of the governing dimensionless parameters on the velocity, temperature, nanoparticle concentration, and magnetic induction profiles. In addition to the graphical results presented in Figures 2–20, the quantitative behavior of important engineering quantities such as the skin friction coefficient, Nusselt number, and Sherwood number is summarized in Tables 2–5.

These engineering quantities provide insight into the surface shear stress, heat transfer rate, and nanoparticle mass transfer rate at the cylinder surface.

The parameter ranges used in the figures and tables are physically realistic and literature-consistent: Casson parameter $\beta = (0, \infty)$; slip $\varsigma = (0, 1)$; curvature $\gamma = (0, 1)$; Chandrasekhar number $Q = (0, 5)$; velocity ratio $\Omega = (0, 1)$; Richardson number $R_i = (0, 2)$; Biot number $Bi = (0.1, 1)$; anisotropic porous parameter $\Gamma = (0, 2)$; Darcy number $Da = (0, 1)$; radiation parameter $R_d = (0, 0.2)$; Eckert number $Ec = (0, 0.04)$; unsteadiness parameter $A_t = (0, 0.7)$; Brownian and thermophoresis $N_b, N_t = (0.01, 0.05)$; Prandtl number $Pr = (0.72, 10)$; suction/injection $f_w = (-0.1, 0.1)$; heat generation/absorption $G = (-0.1, 0.1)$; temperature exponent $\varpi = (0, 2)$; chemical reaction $\kappa^2 = (0, 5)$; Schmidt number $Sc = (1, 5)$; Lewis number $Le = (1, 10)$; and inverse magnetic Prandtl number $\Lambda = (0.1, 10)$. These ranges ensure numerical stability and correspond to realizable thermal, biomedical, and MHD flow systems. To validate the applicability of the homotopy perturbation method (HPM) to the present problem, we found no study addressing the same model, particularly the slip boundary conditions. We therefore adopted the boundary conditions as stated in Ref. [24] and the results were in tandem with their results as can be seen in Table 1.

4.1. Validation of the model

Before discussing the parametric effects, the accuracy of the present formulation is verified by comparing the obtained results with previously published solutions for special cases. When the curvature parameter, Casson parameter, magnetic field, porous resistance, radiation, and other physical mechanisms are neglected, the governing equations reduce to the classical stretching sheet problem analyzed by Ref. [11]. In this limiting case, the analytical solution

$$f(\eta) = 1 - e^{-\eta} \text{ and } \theta(\eta) = \frac{\Gamma(P_r, P_r e^{-\eta})}{\Gamma(P_r, P_r)}, \quad \text{where } \Gamma(a, x) = \int_0^x t^{a-1} e^{-t} dt \tag{51}$$

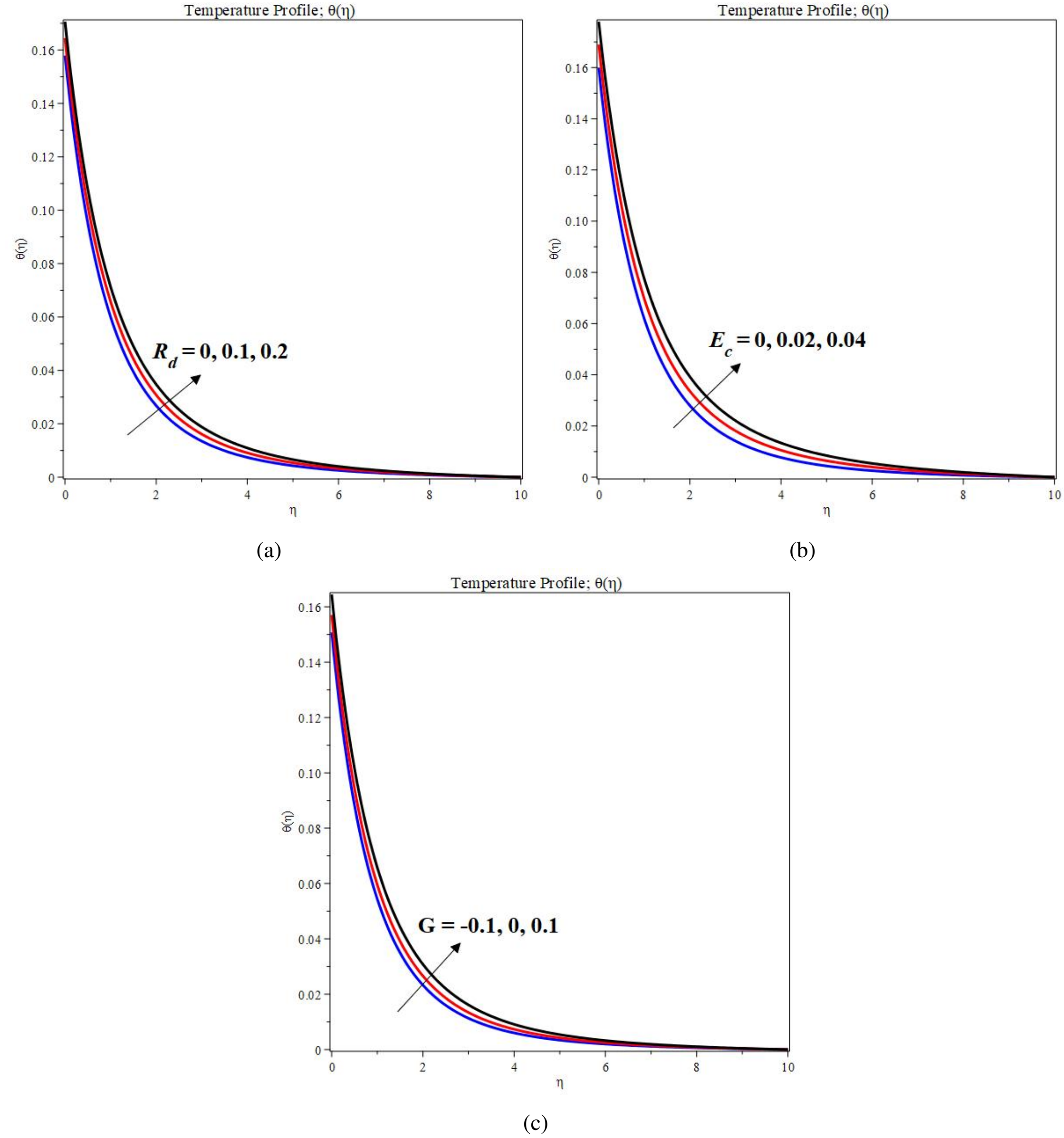

Figure 17: Variation of the temperature profile with the radiation parameter R_d, Eckert number Ec, and heat generation/absorption parameter G.

is the lower incomplete gamma function, yielding $f''(0) = -1$ exactly. The present results show excellent agreement with the classical solution, confirming the validity of the mathematical formulation and the reliability of the semi-analytical solution method.

A comprehensive analysis of the flow, thermal, and mass transport characteristics of the Casson nanofluid system is presented below. The graphical results (Figures 2–20) illustrate the behavior of velocity, temperature, nanoparticle concentration, and magnetic field profiles, while Tables 1–5 provide quantitative insight into the corresponding engineering quantities, namely the skin friction coefficient, Nusselt number, and Sherwood number.

A consistent relationship is observed between the boundary layer profiles and the engineering quantities reported in the tables. Specifically, any parameter that alters the thickness of the velocity, thermal, or concentration boundary layers in the figures directly influences the corresponding surface transport quantities in the tables.

Table 1 presents a validation of the present semi-analytical Homotopy Perturbation Method (HPM) by comparing the computed wall shear stress, wall temperature, and nanoparticle concentration gradients with the corresponding results reported by Ref. [24]. Although the physical model considered by Makkar *et al.* shares many similarities with the present formulation, the two studies are not identical, particularly with respect to the imposed boundary conditions and certain modelling assumptions. Consequently, an exact comparison cannot be expected. To en-

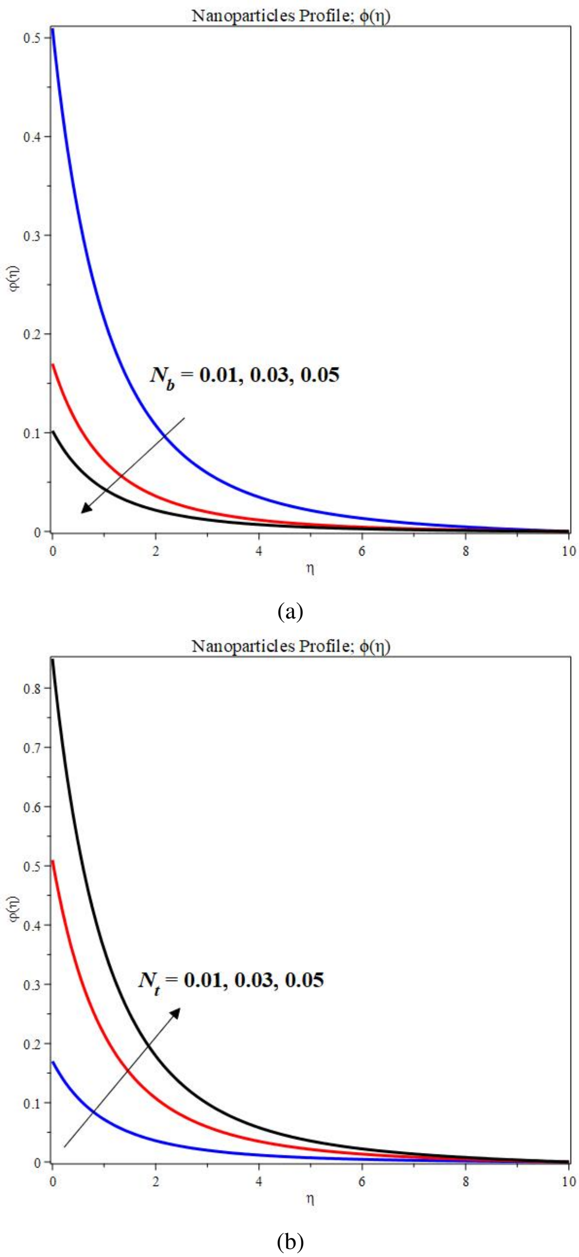

Figure 18: Effects of the Brownian-motion parameter N_b and thermophoresis parameter N_t on the nanoparticle-concentration profiles.

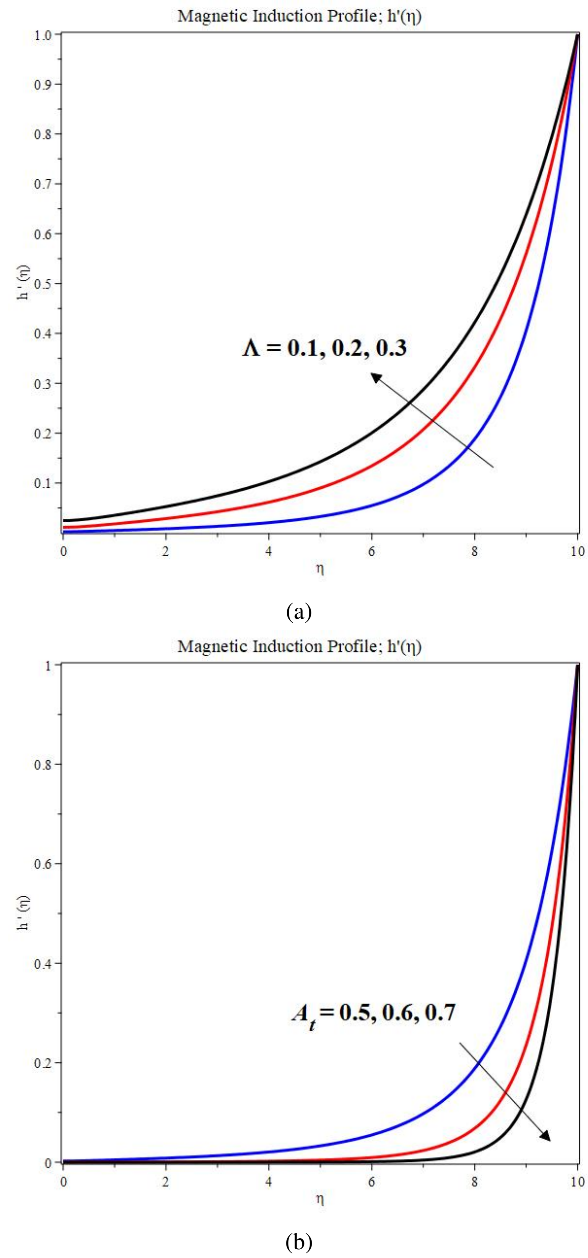

Figure 19: Effects of the inverse magnetic Prandtl number and transient unsteadiness parameter on the magnetic-field profiles.

sure a meaningful assessment of the accuracy of the proposed solution technique, the present governing equations were also solved numerically using Maple's built-in `dsolve` boundary-value solver under the same boundary conditions employed in the current study, and the numerical solutions were subsequently compared with the HPM results.

The results presented in Figure 1 demonstrate an excellent agreement between the HPM solutions and those obtained using the Maple numerical solver, with the relative errors remaining very small for all the investigated parameter combinations. Furthermore, the comparison with the corresponding results of Ref. [24] reveals a close agreement despite the differences in the mathematical formulation and boundary conditions. The minor discrepancies observed are therefore attributed to these differences rather than deficiencies in the present solution procedure. This close agreement confirms the accuracy, convergence, and reliability of the proposed Homotopy Perturbation Method for solving the highly coupled nonlinear boundary-value problem governing the unsteady MHD Casson nanofluid flow over an inclined permeable cylinder.

4.2. Coupling between velocity field and skin friction

The influence of the governing flow parameters on the velocity distribution and the corresponding skin-friction characteristics is illustrated in (Figure 2a, 3a, 4a, 5a, 7a, 9a, 10a,

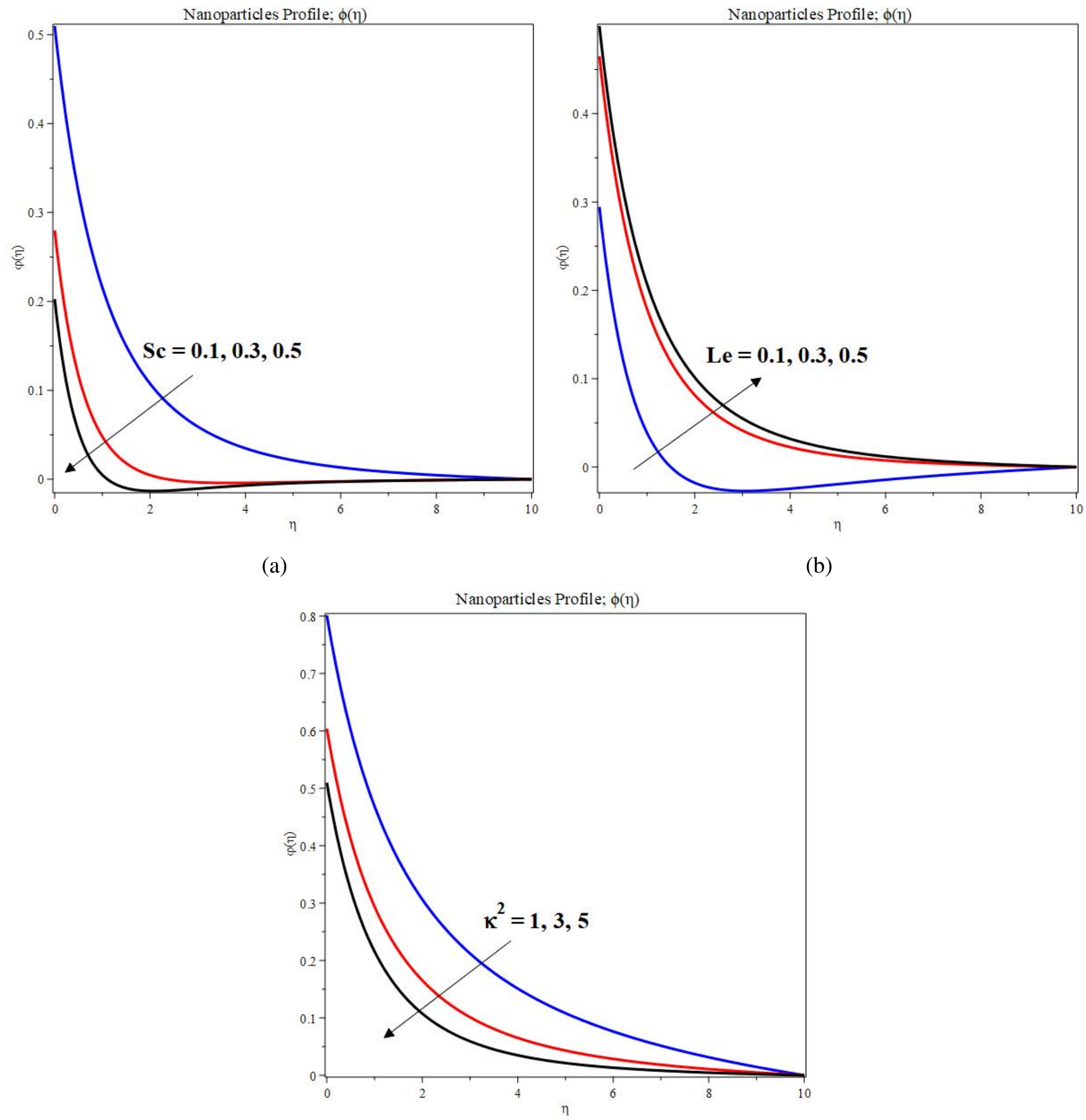

(a)

(b)

(c)

Figure 20: Variation of the concentration profile with the Schmidt number Sc, Lewis number Le, and chemical-reaction parameter κ^2.

11a, 12a, 13a). The transient unsteadiness parameter (A) significantly suppresses the velocity field (Figure 2a). Physically, increasing unsteadiness intensifies the temporal resistance experienced by the fluid, thereby reducing momentum diffusion within the boundary layer. This reduction in velocity is accompanied by a decrease in the momentum boundary-layer thickness and consequently modifies the wall shear stress. The effect of the Casson parameter (β) is presented in Figure 3a. Increasing (β) enhances the velocity profile throughout the boundary layer. Since larger values of (β) correspond to weaker yield-stress effects, the fluid behaves more like a Newtonian fluid and flows more readily. This enhancement of fluid motion is reflected in Figure 3 through the reduction in the magnitude of the skin-friction coefficient.

Figure 4a demonstrates that increasing the suction parameter (f_w) suppresses the velocity profile. Suction removes low-momentum fluid particles from the vicinity of the wall, thereby thinning the hydrodynamic boundary layer. Similarly, the velocity-slip parameter (ζ) shown in Figure 5a increases the velocity distribution because the reduction in wall adhesion allows the fluid to move more freely along the surface. The influence of the curvature parameter (γ) is illustrated in Figure 7a. Larger curvature enhances the velocity profile due to geometric modifications of the cylindrical surface that reduce resistance to flow. In contrast, the Chandrasekhar number (Q) in Figure 9a decreases the velocity profile. This behavior is attributed to the Lorentz force generated by the magnetic field, which opposes fluid motion and acts as a momentum sink. The velocity ratio parameter (Ω) shown in Figure 10a suppresses the velocity profile as the relative strength of the external stream increases. On the other hand, the Richardson number (Ri) in Figure 11a enhances the velocity field because buoyancy forces assist the flow and promote momentum transport. The anisotropic porous-medium parameter (Γ) (Figure 12a) reduces the velocity due to the additional drag imposed by the porous matrix, whereas increasing the Darcy number (Da) (Figure 13a) enhances fluid motion by increasing medium permeability and reducing flow resistance.

These observations are fully consistent with the skin-friction results reported in Tables 3 and 4. Parameters that strengthen resistance to flow, such as (Q) and (Γ), alter the wall shear stress significantly, whereas parameters that facilitate momentum transport, such as (β), (γ), (Ri), and (Da), promote fluid motion and modify the surface drag characteristics. From an engineering perspective, these parameters provide practical mechanisms for controlling momentum transport in polymer extrusion, coating processes, porous thermal systems, and magnetically controlled transport devices.

4.3. Thermal field and heat-transfer rate

The effects of the controlling parameters on the temperature field are depicted in Figures 2b, 3b, 5b, 7b, 9b, 10b, 11b, 12b, 13b, 17a, 14a, 15a, 15c, 16a, 17b, 17c. Figure 2b reveals that increasing the unsteadiness parameter (A) reduces the temperature profile owing to the reduced residence time available for thermal diffusion. A similar decreasing trend is observed with increasing Casson parameter (β) (Figure 3b), where enhanced fluid motion improves convective cooling and lowers the thermal boundary-layer thickness. The slip parameter (ζ) shown in Figure 5b reduces the temperature distribution because slip weakens thermal interaction between the wall and fluid. Likewise, increasing the curvature parameter (γ) decreases the temperature profile (Figure 7b) due to enhanced heat transport away from the cylindrical surface. The magnetic parameter (Q) exhibits the opposite behavior in Figure 9b. Stronger magnetic fields suppress fluid motion and reduce convective cooling, causing thermal energy to accumulate within the boundary layer and increasing the temperature profile. The velocity ratio (Ω), Richardson number (Ri), porous-medium parameter (Γ), and Darcy number (Da) shown in Figures 10b, 11b, 12b, 13b also influence the thermal field through their modification of momentum transport and thermal diffusion processes.

Figure 14a shows that increasing the scaled axial coordinate (Z) decreases the temperature profile. The thermal effects become progressively weaker along the cylinder axis due to continuous diffusion of heat into the surrounding fluid. Figure 15a demonstrates that larger Prandtl numbers reduce the temperature distribution because higher (Pr) corresponds to lower thermal diffusivity. Similarly, increasing the temperature exponent (n) in Figure 15c decreases the thermal boundary-layer thickness. The influence of the Biot number is illustrated in Figure 16a, where larger values of (Bi) significantly enhance the temperature profile. Physically, stronger convective heating at the wall supplies additional thermal energy to the fluid. Figure 17a, 17b, 17c demonstrate that the radiation parameter (R_d), Eckert number (Ec), and heat-generation parameter (G) all increase the temperature distribution. Thermal radiation contributes additional heat flux to the fluid, viscous dissipation converts kinetic energy into thermal energy, and internal heat generation acts as an additional energy source.

These graphical observations agree closely with the Nusselt-number results presented in Tables 3, 4, and 5. Parameters that increase thermal boundary-layer thickness generally reduce the wall temperature gradient and consequently decrease the heat-transfer rate, whereas parameters that thin the thermal boundary layer enhance heat transfer. These findings are particularly important in thermal management systems, nuclear reactors, solar collectors, heat exchangers, and high-temperature manufacturing processes.

4.4. Nanoparticle concentration and mass transfer

The concentration profiles presented in Figures 6a, 8a, 15b, 16b, 18a, 18b, 20a, 20b, 20c reveal the influence of nanoparticle transport mechanisms on mass transfer characteristics. Figure 6a indicates that increasing the slip parameter (ζ) reduces nanoparticle concentration within the boundary layer. The reduction in wall-fluid interaction weakens nanoparticle accumulation near the surface and promotes mass transfer. Figure 8a shows that increasing the curvature parameter (γ) suppresses the concentration profile. This indicates enhanced mass transport away from the surface due to geometric effects associated with the cylindrical configuration. Figure 15b further demonstrates that increasing the Prandtl number decreases nanoparticle concentration because reduced thermal diffusivity weakens the coupled thermal-diffusion mechanisms responsible for nanoparticle transport. The Biot number shown in Figure 16b increases nanoparticle concentration. Enhanced convective heating strengthens thermophoretic transport and promotes nanoparticle accumulation within the thermal boundary layer. The Brownian motion parameter (N_b) in Figure 18a decreases the concentration profile because stronger random particle motion disperses nanoparticles throughout the fluid domain. In contrast, increasing the thermophoresis parameter (N_t) in Figure 18b increases nanoparticle concentration due to the migration of particles from hot regions toward cooler regions of the fluid.

The effects of mass diffusivity and chemical reactions are illustrated in Figure 20. Increasing the Schmidt number (Sc) reduces concentration because mass diffusivity decreases. Similarly, larger Lewis numbers (Le) suppress concentration by weakening nanoparticle diffusion relative to thermal diffusion. Figure 20c shows that increasing the chemical-reaction parameter (κ^2) reduces nanoparticle concentration owing to enhanced consumption of nanoparticles through chemical reaction processes.

These concentration trends are consistent with the Sherwood-number results reported in Figure 5. Parameters that reduce concentration boundary-layer thickness enhance mass transfer at the surface, whereas parameters that increase concentration accumulation reduce the Sherwood number. Such behavior is particularly relevant in catalytic reactors, chemical processing equipment, drying technologies, pollutant transport systems, and nanofluid-based mass transfer devices.

4.5. Interaction of magnetic and thermal effects

The interaction between hydrodynamic motion and magnetic induction is illustrated by the magnetic-field distributions in Figures 2c, 3c, 4c, 6b, 8b, 9c, 10c, 11c, 12c, 13c, 14b, 19a, 19b. Increasing the transient parameter (A) and the Casson parameter (β) enhances the magnetic induction profile, as shown in Figure 2c, 3c, indicating stronger coupling between the conducting fluid and induced magnetic field. Conversely, increasing suction (f_w) reduces the magnetic profile because the removal of conducting fluid weakens magnetic-field generation.

The slip parameter (ζ) shown in Figure 6b strengthens the induced magnetic field by reducing wall resistance and promoting fluid–magnetic interaction. In contrast, increasing the curvature parameter (γ) decreases magnetic induction (Figure 8b), demonstrating the influence of geometry on magnetic diffusion processes.

The effect of the Chandrasekhar number (Q) is particularly significant. Figure 9c shows that stronger magnetic fields considerably increase magnetic induction throughout the boundary layer. The velocity ratio (Ω) suppresses magnetic induction (Figure 10c), whereas buoyancy enhancement through the Richardson number (Ri) increases the magnetic field intensity (Figure 11c). Figures 12c, 13c reveal opposite effects of porous-medium parameters. Increasing (Γ) suppresses magnetic induction because porous resistance weakens fluid motion, whereas larger Darcy numbers enhance magnetic induction owing to increased permeability. Figure 14b shows that the magnetic field weakens along the axial coordinate (Z), indicating gradual magnetic diffusion away from the surface.

Finally, Figure 19 demonstrates the important roles of the inverse magnetic Prandtl number (Λ) and the local transient parameter (A_t). Increasing (Λ) enhances magnetic induction due to reduced magnetic diffusivity, while increasing (A_t) suppresses the magnetic profile by intensifying temporal damping effects. These findings are particularly relevant to electromagnetic pumps, plasma transport devices, liquid-metal cooling systems, and magnetohydrodynamic energy-conversion technologies.

4.6. Effect of surface conditions and boundary parameters

Figures 4, 5, 6, 16 collectively highlight the role of boundary conditions imposed at the cylinder surface. The suction parameter (f_w) acts as a powerful boundary-layer control mechanism. Increasing suction suppresses velocity, temperature, and magnetic induction profiles while reducing the hydrodynamic, thermal, and concentration boundary-layer thicknesses. Consequently, suction can be effectively employed to regulate drag and enhance transport performance in engineering systems.

The velocity-slip parameter (ζ) introduces another important surface effect. Increasing slip enhances the velocity profile while simultaneously reducing temperature and concentration distributions. This behavior results from weakened wall-fluid interaction and reduced momentum and thermal resistance at the surface. Slip surfaces therefore provide a practical means of reducing drag in microfluidic systems and nano-engineered devices.

The convective boundary parameter represented by the Biot number (Bi) strongly affects both thermal and concentration fields. Larger values of (Bi) increase temperature and nanoparticle concentration by strengthening heat exchange between the wall and the surrounding fluid. Consequently, the Biot number serves as an effective parameter for controlling thermal energy delivery in industrial heating and cooling processes.

Overall, the surface parameters (f_w), (ζ), and (Bi) provide efficient mechanisms for manipulating momentum, heat, mass, and magnetic transport simultaneously. Their combined effects offer valuable opportunities for optimizing thermal performance, reducing drag, and improving transport efficiency in advanced nanofluid-based engineering applications.

4.7. Overall physical insight

The combined analysis of Figures 2–20 and Tables 1–5 reveals a strong coupling between the boundary layer profiles and surface transport quantities:

1. Parameters that suppress velocity (e.g., magnetic field, porous resistance) reduce momentum transport and alter heat transfer rates
2. Parameters that increase temperature (e.g., radiation, viscous dissipation) reduce heat transfer efficiency
3. Parameters that enhance nanoparticle diffusion (e.g., Brownian motion, thermophoresis) increase concentration boundary layer thickness and modify mass transfer rates

This unified interpretation highlights the complex interaction between momentum, heat, and mass transport mechanisms in Casson nanofluid flows under magnetohydrodynamic and porous medium effects.

5. Conclusion

This study investigated the coupled thermal and solutal transport characteristics of unsteady induced magnetohydrodynamic Casson nanofluid flow over an inclined permeable cylindrical surface embedded in an anisotropic porous medium. The governing nonlinear partial differential equations describing the conservation of momentum, energy, nanoparticle concentration, and magnetic induction were transformed into a system of nonlinear ordinary differential equations using suitable similarity transformations. The resulting equations were solved using a semi-analytical homotopy perturbation method.

The main findings of the study can be summarized as follows:

- Increasing the magnetic parameter suppresses the velocity distribution due to the resistive Lorentz force while simultaneously increasing the temperature distribution within the boundary layer.

- Higher values of the Casson parameter enhance fluid motion because the yield stress effect becomes weaker, allowing the fluid to flow more easily.
- Suction at the surface significantly reduces the velocity and temperature boundary layer thickness, indicating that suction can be used as an effective technique for controlling heat transfer.
- Thermal radiation and viscous dissipation increase the temperature distribution within the boundary layer, thereby influencing the overall heat transfer characteristics of the system.
- Brownian motion enhances nanoparticle diffusion and increases concentration profiles, whereas thermophoresis drives nanoparticles away from the heated surface.
- Increasing porous medium resistance reduces fluid velocity due to drag effects generated by the porous matrix.

The results obtained in this study provide important insights into the interaction between magnetic fields, porous media, and nanofluid transport mechanisms. These findings may be useful for designing advanced thermal management systems in engineering applications such as heat exchangers, energy transport devices, and chemical processing equipment.

Future studies may consider extending the present analysis to include hybrid nanofluids, variable thermophysical properties, or three-dimensional flow configurations.

Data availability

There are no data available for the study.

Declaration of competing interest

The authors declare that they have no known competing financial or personal interests that could have appeared to influence the work reported in this article.

Funding

The authors received no specific funding from any public, commercial, or not-for-profit organisation for this research.

References

[1] S. U. S. Choi & J. A. Eastman, "Enhancing thermal conductivity of fluids with nanoparticles", Proceedings of the ASME International Mechanical Engineering Congress and Exposition, San Francisco, USA, 1995, pp. 99–105. https://doi.org/10.1115/IMECE1995-0926.

[2] J. Buongiorno, "Convective transport in nanofluids", Journal of Heat Transfer **128** (2006) 240. https://doi.org/10.1115/1.2150834.

[3] W. A. Khan & I. Pop, "Boundary-layer flow of a nanofluid past a stretching sheet", International Journal of Heat and Mass Transfer **53** (2010) 2477. https://doi.org/10.1016/j.ijheatmasstransfer.2010.01.032.

[4] F. Mabood, W. A. Khan & A. I. M. Ismail, "MHD boundary-layer flow and heat transfer of nanofluids over a nonlinear stretching sheet", Journal of Magnetism and Magnetic Materials **374** (2015) 569. https://doi.org/10.1016/j.jmmm.2014.09.013.

[5] Y. X. Li, M. H. Alshbool, Y. P. Lv, I. Khan, M. R. Khan & A. Issakhov, "Heat and mass transfer in MHD Williamson nanofluid flow over an exponentially porous stretching surface", Case Studies in Thermal Engineering 26 (2021) 100975. https://doi.org/10.1016/j.csite.2021.100975.

[6] A. Zhu, H. Ali, M. Ishaq, M. S. Junaid, J. Raza & M. Amjad, "Numerical study of heat and mass transfer for Williamson nanofluid over a stretching/shrinking sheet along with Brownian and thermophoresis effects", Energies **15** (2022) 5926. https://doi.org/10.3390/en15165926.

[7] N. Casson, "A flow equation for pigment-oil suspensions", in Rheology of Disperse Systems, Pergamon Press, Oxford, UK, 1959, pp. 84–102.

[8] S. S. Ghadikolaei, K. Hosseinzadeh, D. D. Ganji & B. Jafari, "Nonlinear thermal radiation effect on magneto Casson nanofluid flow with Joule heating effect over an inclined porous stretching sheet", Case Studies in Thermal Engineering **12** (2018) 176. https://doi.org/10.1016/j.csite.2018.04.009.

[9] A. S. Idowu, M. T. Akolade, J. U. Abubakar & B. O. Falodun, "MHD free convective heat and mass transfer flow of dissipative Casson fluid with variable viscosity and thermal conductivity effects", Journal of Taibah University for Science **14** (2020) 851. https://doi.org/10.1080/16583655.2020.1781431.

[10] K. R. Cramer & S.-I. Pai, Magnetofluid Dynamics for Engineers and Applied Physicists, Scripta Publishing Company, Washington, DC, USA, 1973.

[11] L. J. Crane, "Flow past a stretching plate", Zeitschrift für Angewandte Mathematik und Physik **21** (1970) 645. https://doi.org/10.1007/BF01587695.

[12] A. K. Mishra, P. K. Pattnaik, S. R. Mishra & N. Senapati, "Dissipative heat energy on Cu and Al_2O_3 ethylene-glycol-based nanofluid flow over a heated semi-infinite vertical plate", Journal of Thermal Analysis and Calorimetry **145** (2021) 129. https://doi.org/10.1007/s10973-020-09666-z.

[13] T. Thumma, S. R. Mishra, M. A. Abbas, M. M. Bhatti & S. I. Abdelsalam, "Three-dimensional nanofluid stirring with a non-uniform heat source/sink through an elongated sheet", Applied Mathematics and Computation **421** (2022) 126927. https://doi.org/10.1016/j.amc.2022.126927.

[14] S. Panda, S. Ontela, S. R. Mishra & P. K. Pattnaik, "Response surface methodology and sensitivity analysis for optimizing the heat-transfer rate in three-dimensional hybrid nanofluid flow through a permeable stretching surface", Journal of Thermal Analysis and Calorimetry **148** (2023) 7369. https://doi.org/10.1007/s10973-023-12183-4.

[15] P. P. Humane, V. S. Patil & A. B. Patil, "Chemical reaction and thermal radiation effects on magnetohydrodynamic flow of Casson–Williamson nanofluid over a porous stretching surface", Proceedings of the Institution of Mechanical Engineers, Part E: Journal of Process Mechanical Engineering **235** (2021) 2008. https://doi.org/10.1177/09544089211025376.

[16] P. K. Pattnaik, S. R. Mishra, S. Panda, S. A. Syed & K. Muduli, "Hybrid methodology for the computational behaviour of thermal radiation and chemical reaction on viscoelastic nanofluid flow", Mathematical Problems in Engineering **2022** (2022) 2227811. https://doi.org/10.1155/2022/2227811.

[17] S. Tinker, S. R. Mishra, P. K. Pattnaik & R. P. Sharma, "Simulation of time-dependent radiative heat motion over a stretching/shrinking sheet of hybrid nanofluid: stability analysis for dual solutions", Proceedings of the Institution of Mechanical Engineers, Part N: Journal of Nanomaterials, Nanoengineering and Nanosystems **236** (2022) 19. https://doi.org/10.1177/23977914211069021.

[18] S. Baag & S. Panda, "Free convection of conducting nanofluid past an expanding surface with heat source with convective heating boundary conditions", International Journal of Ambient Energy **44** (2023) 880. https://ui.adsabs.harvard.edu/abs/2023IJAmE..44..880B/abstract.

[19] N. Gomathi & D. Poulomi, "Entropy optimization on EMHD Casson–Williamson penta-hybrid nanofluid over porous exponentially vertical cone", Alexandria Engineering Journal **108** (2024) 590. https://doi.org/10.1016/j.aej.2024.07.092.

[20] M. Sadighi, S. E. Ghasemi & M. Hatami, "Magnetohydrodynamic nanofluid flow over a stretching surface with thermal radiation and chemical reaction", Case Studies in Thermal Engineering **41** (2023) 103345. https://doi.org/10.1016/j.csite.2023.103345.

[21] S. Irshad, S. Jahan, J. M. Machado, P. Śliwiński, K. Kędzia & A. Z. Jan, "MHD Casson flow across a stretched surface in a porous material: a numerical study", Multiscale and Multidisciplinary Modeling, Experiments

and Design **8** (2025) 36. https://doi.org/10.1007/s41939-024-00628-8.

[22] T. A. Walelign, "Casson nanofluid flow over a stretching surface with thermal radiation and magnetic-field effects", Results in Engineering **23** (2025) 101850. https://www.researchgate.net/publication/354983698.

[23] K. A. Abbas, K. M. Naveed, N. A. Ahammad, M. Ashraf, K. Guedri & A. M. Galal, "Flow investigation of second grade micropolar nanofluid with porous medium over an exponentially stretching sheet", Journal of Applied Biomaterials & Functional Materials **2022** (2022) 20. https://doi.org/10.1177/22808000221089782.

[24] V. Makkar, V. Poply & N. Sharma, "Radiative MHD non-Newtonian chemically reactive nanofluid flow with a heat source induced by a nonlinear stretching cylinder", Trends in Sciences **19** (2022) 6314. https://doi.org/10.48048/tis.2022.6314.

[25] E. M. A. Elbashbeshy, "Heat transfer over a stretching surface with variable surface heat flux", Journal of Physics D: Applied Physics **31** (1998) 1951. https://doi.org/10.1088/0022-3727/31/16/002.

[26] N. Bachok, A. Ishak & I. Pop, "Flow and heat transfer over a stretching/shrinking sheet in a nanofluid", Advances in Mechanical Engineering **2** (2010) 681345.

[27] N. A. Mat Noor, S. Shafie & M. A. Admon, "Unsteady MHD flow of Casson nanofluid with chemical reaction, thermal radiation and heat generation/absorption", MATEMATIKA: Malaysian Journal of Industrial and Applied Mathematics **35** (2019) 33. https://doi.org/10.11113/matematika.v35.n4.1262.

[28] H. A. Attia, "Hiemenz flow through a porous medium of a non-Newtonian Rivlin–Ericksen fluid with heat transfer", Journal of Applied Science and Engineering **12** (2009) 359. http://163.13.100.126/articles/jase-200909-12-3-15.pdf.

[29] K. G. Kumar, B. J. Gireesha & M. G. Reddy, "MHD flow and heat transfer of Casson nanofluid over a stretching sheet with Joule heating and thermal radiation", Journal of Molecular Liquids **276** (2019) 653. https://www.researchgate.net/publication/343417335.

[30] A. Adeniyan, F. Mabood & S. S. Okoya, "Effect of heat radiating and generating second-grade mixed-convection flow over a vertical slender cylinder with variable physical properties", International Communications in Heat and Mass Transfer **121** (2021) 105110. https://doi.org/10.1016/j.icheatmasstransfer.2021.105110.

[31] T. M. Kabir & T. Abdulganiyu, "Homotopy perturbation method for analyzing the effect of viscous dissipation on steady natural-convection Couette flow with convective boundary conditions", International Journal of Fluid Mechanics & Thermal Sciences **10** (2024) 45. https://doi.org/10.11648/j.ijfmts.20241003.11.

[32] A. J. Shkarah, S. W. Noori, D. A. Lafta, A. M. Lafta & M. M. Mansour, "Application of the homotopy perturbation method to the Jeffery–Hamel flow of nanofluids between two non-parallel planar walls", Results in Engineering **28** (2025) 107805. https://doi.org/10.1016/j.rineng.2025.107805.